

This article should be cited as:

A. Weathers, L. Shi, "Thermal Transport Measurement Techniques for Nanowires and Nanotubes," Annual Review of Heat Transfer, Vol. 16, pp. 101-134, ed. G. Chen, DOI: 10.1615/AnnualRevHeatTransfer.v16.40, Begell House (2013)

Thermal Transport Measurement Techniques for Nanowires and Nanotubes

Annie Weathers and Li Shi*

Department of Mechanical Engineering, The University of Texas at Austin, Austin, TX 78712, USA

*Address all correspondence to Li Shi E-mail: lishi@mail.utexas.edu

Recent advances in the synthesis of inorganic and organic nanowires and nanotubes have provided both components for various functional devices and platforms for the study of low-dimensional transport phenomena. However, tremendous challenges have remained not only for the integration of these building blocks into functional devices, but also in the characterization of the fundamental transport properties in these nanoscale model systems. In particular, thermal and thermoelectric transport measurements can be considerably more complicated than electron transport measurements, especially for individual nanostructures. During the past decade, a number of experimental methods for measuring the thermal and thermoelectric properties of individual nanowires and nanotubes have been devised to address these challenges, some of which are reviewed and analyzed in this chapter. Although the Seebeck coefficient and electrical conductivity can also be obtained from some of the measurement methods, this chapter is focused on measurement techniques of the thermal conductivity and thermal diffusivity of nanowires and nanotubes. It is suggested that the limitations in the current experimental capability will provide abundant opportunities for innovative approaches to probing fundamental thermal and thermoelectric transport phenomena in individual nanostructures.

1 Introduction

Nanowire (NW) and nanotube structures have been explored as building blocks for electronic, photonic, thermoelectric, and thermal management devices.^{1–3} For example, bottom-up synthesized semiconducting NWs and carbon nanotubes have been employed as the conducting channel in field-effect transistors (FETs).^{4–7} Meanwhile, the nanoscale channel in top-down patterned Si FinFETs is essentially a NW.^{8,9} In nanoelectronic devices, the high and nonuniform heat dissipation density and the resulting local hotspots are detrimental to device performance and reliability, and present a major challenge. Phonon scattering by interface roughness can considerably reduce the effective thermal conductivity of nanostructures including NWs, and is one of the causes of the local hotspots in nanoelectronic devices.^{10,11}

However, the reduced thermal conductivity in NWs and other nanostructured materials is desirable for thermal insulation and thermoelectric materials. Thermoelectric materials are characterized by their dimensionless figure of merit, $ZT = S^2\sigma T/\kappa$, where S is the Seebeck coefficient, σ is the electrical conductivity, T is the absolute temperature, and κ is the thermal conductivity that consists of a lattice or phonon contribution (κ_L) and an electronic contribution (κ_e). The best thermoelectric materials will therefore have low thermal conductivity, and high electrical conductivity and Seebeck coefficient. However, engineering such a material is nontrivial due to the substantial coupling between these three parameters. For example, increasing the charge carrier concentration via doping can be used to increase the electrical conductivity, but often decreases the Seebeck coefficient, and increases the electronic contribution to the thermal conductivity. Consequently, the highest ZT values reported for bulk single crystals have been limited to be close to unity. In recent years, there have been a number of investigations of nanostructuring to enhance thermoelectric performance. The suppressed lattice thermal conductivity in nanostructures can help to increase the ZT, when the power factor ($S^2\sigma$) is not suppressed as much as the lattice thermal conductivity.¹² This is possible when the interface or boundary scattering mean free path in the nanostructures is shorter than the phonon mean free path in the bulk crystal but longer or comparable to the bulk electron mean free path. In this case, it is possible for the phonon mean free path and thermal conductivity to be reduced more than the electron mean free path and electrical conductivity, respectively.

In addition to the classical effects of interface scattering, there have also been a number of theoretical studies of the quantum size effects on the thermoelectric power factor ($S^2\sigma$). As one of the first theoretical

studies, Hicks and Dresselhaus¹³ examined thermoelectric transport in 1D Bi₂Te₃ quantum wires, for which the wire diameter is comparable to or smaller than the de Broglie wavelength of electrons. The electronic density of states in such quantum wires can be highly asymmetric around the Fermi energy, which can result in an enhanced power factor.^{14,15}

Similarly, as the diameter of the NW is reduced further below the dominant wavelength of thermal phonons, ranging from on the order of 1 nm at room temperature to tens of nanometers at low temperatures, there exist only a few 1D phonon sub-bands with well separated wave vector components along the radial direction of the NW. Because of the requirement of energy and momentum conservation in phonon-phonon scattering, some of the phonon-phonon scattering events allowable in bulk crystals are eliminated in quasi-1D NWs because of the modified phonon dispersion. In conjunction with an atomically smooth surface, the suppressed phonon-phonon scattering may reverse the dependence of the lattice thermal conductivity on the diameter of nanowires, and can lead to increasing thermal conductivity with decreasing diameter, when the diameter is reduced below a threshold value on the order of the phonon wavelength.¹⁶ Carbon nanotubes and polymer fiber chains are two representative examples of such quasi-1D systems of potentially high thermal conductivity that is desirable for thermal management applications.

Therefore, recent advances in the synthesis of inorganic and organic NWs and nanotubes have provided both components for various functional devices and a platform for the study of low-dimensional transport phenomena. However, tremendous challenges have remained not only for the integration of these building blocks into functional devices, but also in the characterization of the fundamental transport properties in these nanoscale model systems. In particular, thermal and thermoelectric transport measurements can be considerably more complicated than electron transport measurements, even in bulk samples. For example, issues such as radiation loss, heat loss to the thermometers, and contact thermal resistance can lead to large uncertainty in thermal conductivity measurements. To emphasize these complications, Tye¹⁷ wrote in the preface of a 1969 text on thermal conductivity that “the situation has not been helped when poor experimental work had led to suggestions that new transport mechanisms exist, only for them to be eliminated by a later more careful experimental investigation.” If issues already existed in the thermal measurements of bulk size samples, these issues can become pronounced in nanostructure samples of a much smaller dimension, especially individual NWs and nanotubes that are difficult to handle and require miniaturized thermometers in the measurements.

During the past decade, a number of experimental methods for measuring the thermal and thermoelectric properties of individual NWs and nanotubes have been devised to address these challenges. Some of these methods are reviewed and analyzed in this chapter. As summarized in Table 1, these methods include those based on NW samples with a steady state temperature difference applied to the two ends, such as measurements based on suspended resistance thermometer microdevices and bimaterial cantilever thermal sensors. In addition, several techniques based on electrical self-heating and optical heating of the NW samples have been reported, including the celebrated 3ω method and other steady state or pulsed heating techniques. Besides electrical resistance thermometry, optical non-contact thermometry techniques including micro-Raman spectroscopy and time domain thermoreflectance (TDTR) measurements have been explored for thermal measurements of individual NWs, nanotubes, and NW arrays. Although the Seebeck coefficient and electrical conductivity can also be obtained from some of the measurement methods, this chapter is focused on measurements of the thermal conductivity and thermal diffusivity for NWs and nanotubes.

2 Suspended Mesa Structures for Thermal Conductance Measurements of Suspended Beams

One of the first thermal measurements of nanostructures was reported by Tighe et al.,¹⁸ who developed a method of measuring the thermal conductance of patterned, suspended GaAs nanobeams in the temperature range of 1.5 - 6 K. The measurement device was patterned from a wafer composed of three layers, i.e., a topmost conducting layer of heavily doped GaAs from which a serpentine heater and electrodes were patterned, a middle undoped GaAs layer from which the central thermal reservoir and GaAs nanobeams were defined, and finally a sacrificial AlAs layer. Figures 1(a) and 1(b) show an image of the measurement device, which has the four supporting GaAs nanobeams with the cross-sectional dimension of 200 × 300 nm. The thermal conductance was obtained by supplying a direct current (DC) heating to one of the serpentines on the central membrane and monitoring the membrane temperature rise with a small modulated sensing current

Techniques	Heating Method	Sensing Method	κ	α	C_p	σ, S
Suspended mesa structure	Steady state end heating	Noise thermometry	x			
Suspended resistance thermometer device	Steady state end heating	Resistance thermometry	x			x
T-junction sensor	Steady state end heating	Resistance thermometry	x			
Bimaterial cantilever sensor	Steady state end heating	Cantilever deflection	x			
Cantilever resistance thermometry	Steady state end heating	Resistance thermometry	x	x		
3ω	Modulated self-electrical heating	Resistance thermometry	x	x	x	x
Transient electrothermal techniques	Pulsed electrical or optical heating	Resistance thermometry	x	x		
Micro-Raman spectroscopy	Optical absorption or self-electrical heating	Raman peak shift	x			
Time domain thermoreflectance	Optical heating	Thermoreflectance	x	x		

Table 1: Summary of thermal measurement techniques for nanowires and nanotubes. κ , α , C_p , σ , and S refer to the thermal conductivity, thermal diffusivity, specific heat, electrical conductivity, and Seebeck coefficient of the sample. The 'x' indicates the property that was obtained by each technique.

through the other serpentine resistance thermometer. The thermal conductance, $G = Q/\Delta T$, was obtained from the measured DC heating rate, Q , and the temperature rise of the heating membrane determined from the sensing voltage.

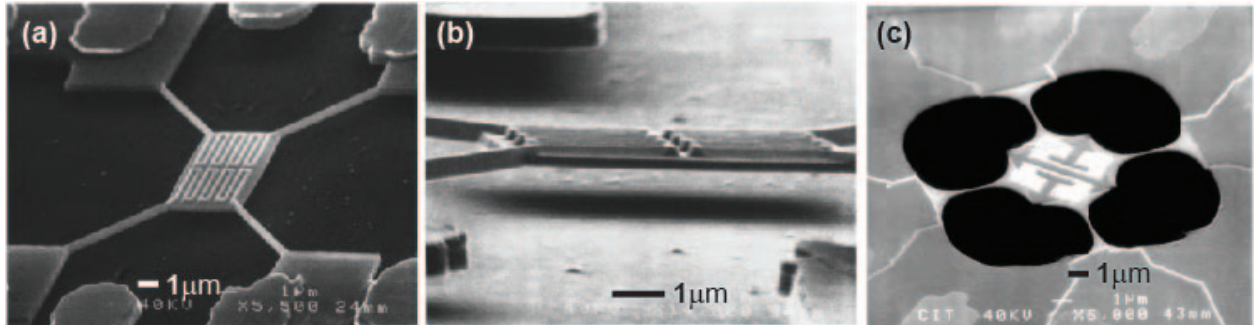


Figure 1: (a,b) SEM images of the measurement device from Tighe et al.¹⁸ with four patterned GaAs nanobeams supporting a central GaAs membrane with serpentine resistance heater and thermometer patterned on top. (c) SEM image of the device of Schwab et al.¹⁹ used to measure the quantum of thermal conductance, with a central SiN_x membrane supported by four SiN_x beams with Nb leads on top. (a,b) Reprinted with permission from Tighe et al.¹⁸ Copyright 1997, American Institute of Physics. (c) Reproduced from Schwab et al.¹⁹ with permission from Macmillan Publishers Ltd: Nature. Copyright 2000.

A similar device was used to measure the quantum of thermal conductance of SiN_x nanoconstrictions by Schwab et al.¹⁹ Their device consisted of a SiN_x central membrane with four supporting SiN_x beams, a patterned Cr/Au serpentine heater and sensor, and four Nb leads, as shown in Fig. 1(c). The SiN_x nanoconstrictions were patterned with a $\cosh^2 x/\lambda$ geometry, where x is the lateral coordinate along the lead and λ was designed to be $1 \mu\text{m}$. Such a geometry was intended to achieve a transmission coefficient close to unity for long-wavelength phonons, which dominate thermal transport at temperatures of $< 1 \text{ K}$. In addition, at temperatures of $< 9.2 \text{ K}$, the Nb leads become superconducting and therefore generate no electrical heating in the supporting beams. The electron temperature of the Au film was obtained by measuring its Johnson noise at a minimum power with the use of a sensitive superconducting quantum

interference device (SQUID).²⁰ Below a cutoff temperature of ~ 800 mK, when only the four lowest-lying modes are excited, they found a plateau in the thermal conductance corresponding to $16g_0$, where g_0 is the quantum of thermal conductance, $\pi^2 k_B^2 (T/3h)$,²¹ and the factor of 16 arises because of the four SiN_x phonon waveguides each with four 1D branches, including one longitudinal, two transverse, and one torsional branch. At this cutoff temperature, the dominate phonon wavelength is comparable to the dimensions of the nanoconstrictions, which is 200 nm at its smallest dimension.

3 Suspended Resistane Thermometer Microdevices for Thermal and Thermoelectric Measurements of Suspended Nanowires and Nanotubes

Shi,²² Kim et al.,²³ and Shi et al.²⁴ fabricated a suspended platinum resistance thermometer (PRT) device for measuring the thermal conductivity of individual carbon nanotubes. The device was later used by Li et al.²⁵ for the thermal measurement of Si NWs and by Mavrokefalos et al.²⁶ for the measurement of InAs thin films. The device consists of two adjacent thermally isolated SiN_x membranes supported by long SiN_x beams, as shown in Figs. 2(a) and 2(b). A Pt thin film serpentine is patterned on each SiN_x membrane, and was connected to four Pt leads allowing for four-probe measurement of the resistance of the serpentine. In recent designs, two electrodes were patterned on each membrane for measurements of the Seebeck coefficient and the electrical conductivity of the samples.^{26,27} The membranes and SiN_x beams were suspended above a through-substrate hole, which allowed for transmission electron microscopy (TEM) characterization of the nanostructure sample assembled on the membrane.

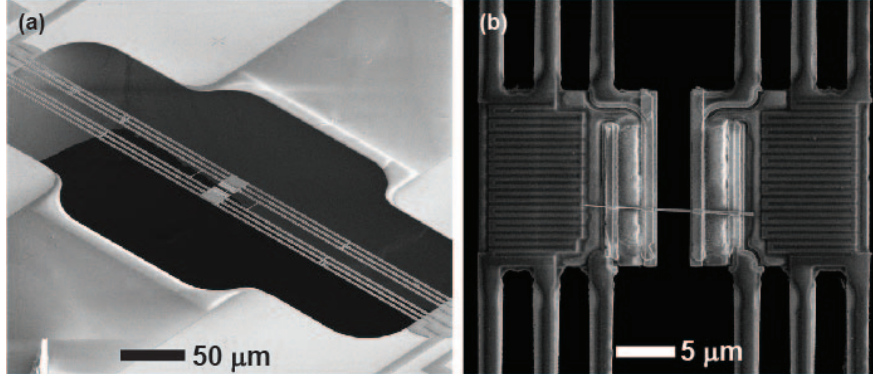


Figure 2: SEM images of (a) the suspended device used for thermal and thermoelectric measurements of individual NWs and (b) an InAs NW with Ni/Pd evaporated on the four contacts through a SiN_x shadow mask.

3.1 Sample Preparation

Several methods have been used to place a NW across the two suspended membranes of the resistance thermometer device. One method involves dispersing the NWs in a solvent and drop casting the suspension onto a wafer containing many of the suspended devices. Occasionally, one NW is trapped between the two membranes of a suspended device. This method requires a NW suspension with sufficiently high NW density in order to achieve a good assembly yield. In another method, a tungsten probe attached to a micromanipulator can be used to manually pick up the NW and place it across the device. This may be achieved either with a nanomanipulator inside the vacuum chamber of a scanning electron microscope (SEM), or simply with a home-built micromanipulator stage underneath an optical microscope. The process is clean and leaves no solvent residue on the NW surface. However, this method is not effective for some fragile NW materials. In addition, the adhesion between the NW and SiN_x/Pt membrane is weak compared to the sample prepared with the drop-casting method, where residue or moisture left by the solvent helps to enhance the adhesion between the nanostructure and the two membranes.²⁸

Another challenge in the sample preparation procedure is making electrical contact between the NW and the Pt electrodes patterned at the edge of each SiN_x membrane. The presence of native oxide on

the surface of a NW can prevent direct electric contact between the assembled NW and the underlying Pt electrodes on the two SiN_x membranes. Mavrokefalos et al.²⁹ have shown that annealing in a forming gas containing 5% hydrogen in nitrogen was able to reduce the surface oxide of a Bi_2Te_3 NWs assembled on the suspended device so as to obtain ohmic electrical contact between the NW and the Pt electrodes without any deposited metal. However, this method has not been effective for other NW materials. Focused ion beam (FIB)-assisted deposition and electron beam-induced deposition (EBID) of Pt/C can be used to make electrical contact and improve the thermal contact to a variety of suspended NWs, as shown by a number of works.^{27,30–34} However, it has been shown that there is considerable spreading of the Pt-C within a 5 μm radius of the electron beam spot during EBID.³⁵ To reduce the influence of metallic contamination of the nanowire surface, Tang et al.³⁶ have evaporated Ni through the windows of a SiN_x shadow mask directly onto the two contacts between a porous Si film and the two suspended membranes. Because of the presence of native oxide on the Si film, the evaporated metal did not make electrical contact to the sample. In another work, Weathers et al.³⁷ succeeded in depositing metal contacts through a shadow mask to make electrical contact to an InAs NW assembled on the suspended device shown in Fig. 2(b), and etched in BCl_3 plasma before deposition. Further efforts along this direction can potentially lead to reliable, clean contact between different NWs and the suspended devices.

3.2 Two-Probe Thermal Measurement Procedure

The thermal conductance of a suspended NW can be obtained by electrically heating one PRT and monitoring the temperature rise of the two SiN_x membranes. During the thermal measurement, the sample is placed in a variable-temperature cryostat. Heat transfer to the surrounding gas molecules is minimized by evacuating the sample space of the cryostat to a vacuum level better than 10^{-5} torr with the use of a turbomolecular pump. When the internal thermal resistance of each membrane is much smaller than the thermal resistance of the supporting beams and that of the sample, the temperature on each membrane is uniform, as verified by numerical heat transfer analysis.^{38,39} The radiation loss from the circumference of the long supporting

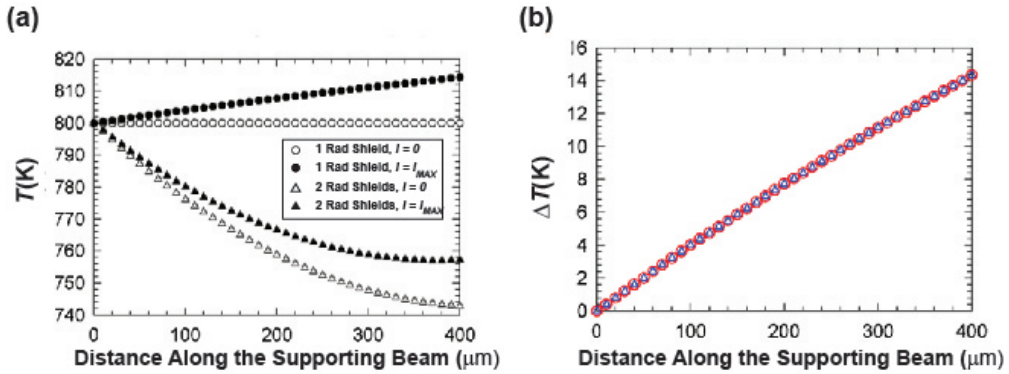


Figure 3: (a) Temperature profile along the supporting SiN_x beams with and without electrical heating and with one and two radiation shields, for $T_0 = 800$ K. (b) The difference in temperature $\Delta T = T(I) - T(I = 0)$ for one (triangles) and two (circles) radiation shields. The additional shield in the two-shield configuration is thermally anchored to the sample stage. Compared to the nonlinearity in the temperature profile for the absolute temperature, the difference in temperature is essentially linear. Reproduced from Moore and Shi³⁹ with permission from IOP Publishing. Copyright 2011.

beams can be accounted for in the heat diffusion equation given by

$$\frac{d^2T}{dx^2} + \frac{\dot{q}}{\kappa_b} = \frac{\sigma\epsilon P(T^4 - T_0^4)}{\kappa_b A_b} \quad (1)$$

where x is measured from the junction between the substrate and the SiN_x beam, κ_b , L_b , A_b , P , and \dot{q} are the thermal conductivity, length, cross section, perimeter, and the volumetric heating rate of the supporting beam, respectively, ϵ and σ are the emissivity of the sample and the Stefan-Boltzmann constant, and T_0 is the temperature of the environment enclosing the sample. The ratio between the radiative and conductive heat transfer through the supporting beam, Q_{rad}/Q_{cond} , can be found by multiplying the right-hand side of

Eq. (1) by $L_b^2/\Delta T_{x=0 \rightarrow L}$, where $\Delta T_{x=0 \rightarrow L}$ is the temperature difference between the two ends of the beam. Because of the large thermal resistance ($L_b/\kappa_b A_b$) of the supporting beams for each membrane, on the order of 10^7 K/W, this term is not negligible when T_0 differs significantly from the average temperature of the beam. The effects of radiation loss can be clearly seen in Fig. 3(a), calculated by Moore et al.³⁹ by finite element modeling, which shows that the use of one radiation shield yields a highly nonlinear temperature profile of the beam supporting the sensing membrane at a high $T_0 = 800$ K. As one important consequence, the sensing membrane temperature T_s can be almost 60 K lower than T_0 when no electrical heating ($I = 0$) is supplied to the heating membrane.

However, the nonlinearity in the temperature profile can be overcome by considering instead the change in temperature between nonzero heating current, I , and zero heating current, $I = 0$. Subtracting Eq. (1) for $I = 0$ from the same equation for $I \neq 0$ gives

$$\frac{d^2\Delta T}{dx^2} + \frac{\dot{q}}{\kappa_b} = \frac{\sigma\epsilon P}{\kappa_b A_b} (T(I)^4 - T(I = 0)^4) \quad (2)$$

where $\Delta T(x) \equiv T(x, I) - T(x, I = 0)$. During measurements, ΔT is usually kept at < 10 K for $T_0 > 300$ K and at < 5 K for lower temperatures. Consequently, the $T(x, I)^4 - T(x, I = 0)^4$ term is considerably smaller than $T(x, I)^4 - T_0^4$ for the case of inadequate radiation shielding. As a result, the $\Delta T(x)$ profile obtained from the numerical analysis of Moore et al.³⁹ with radiation loss taken into account is nearly linear, even for the case of only one radiation shield and the sample stage temperature at $\Delta T_0 = 800$ K, as shown in Fig. 3(b).

With the additional radiation loss term in the right-hand side of Eq. (2) ignored, a current I to the heating membrane results in additional heat conduction $\Delta Q = \kappa_b A_b \Delta T(L)/L_b$ to the substrate from each supporting beam without the heating current, and $\Delta Q = \kappa_b A_b \Delta T(L)/L_b + Q_l/2$ for each beam carrying a DC heating current, where $Q_l = I^2 R_l$, and R_l is the electrical resistance of the Pt lead on the SiN_x beam. Because the temperature is uniform on each of the two membranes, $T(x = L)$ is equal to T_h and T_s for the supporting beams of the heating and sensing membranes, respectively. With the additional radiation loss ignored, $Q_h + 2Q_l = 6(\kappa_b A_b/L_b)(\Delta T_h + \Delta T_s) + Q_l$, where $\Delta T_h \equiv T_h(I) - T_h(I = 0)$ and $\Delta T_s \equiv T_s(I) - T_s(I = 0)$. Therefore, the thermal resistance of the six supporting beams for each membrane is

$$R_b = \frac{\Delta T_h + \Delta T_s}{Q_h + Q_l} \quad (3)$$

The ratio of radiation loss from the suspended NW to the heat conduction through the NW is proportional to L^2/d , where L and d are the suspended length and diameter of the suspended NW, respectively. When L is on the order of $10 \mu\text{m}$ or shorter, radiation loss is negligible compared to heat conduction through most NW materials even at temperatures as high as 800 K, as shown in Ref. 39.

In addition to radiation loss, there also exists a thermal contact resistance between the NW and the SiN_x membrane. A resistance circuit including this contact resistance is presented in Fig. 4 together with a characteristic temperature profile along the nanowire. The two-probe thermal resistance of the sample can then be obtained from

$$R_{total} = R_S + R_{c1} + R_{c2} = R_b \frac{\Delta T_h - \Delta T_s}{\Delta T_s} \quad (4)$$

where R_S refers to the intrinsic thermal resistance of the sample, and R_{c1} and R_{c2} are the contact thermal resistances to the two ends of the NW. The temperature rise of the membranes, ΔT_h and ΔT_s , are obtained by measuring the electrical resistance of the two PRTs. At different heating current (I) supplied to the heating PRT, the four-probe electrical resistance (R_s) of the sensing PRT can be measured with a sinusoidal current from a lock-in amplifier. The temperature rise of the sensing membrane is obtained as

$$\Delta T_s(I) \equiv \frac{\Delta R_s}{dR_s(I = 0)/dT} \quad (5)$$

where $\Delta R_s = R_s(I) - R_s(I = 0)$, and the temperature coefficient of resistance, $dR_s(I = 0)/dT$, of the PRT must be determined accurately from the measured $R_s(I = 0)$ versus $T_s(I = 0)$ curve. As discussed above, with inadequate radiation shielding or at high or low temperatures, $T_s(I = 0)$ deviates considerably from the sample stage temperature T_0 , which is measured with a temperature sensor attached to the sample stage. Thus, although Eqs. (3) and (4) are still accurate for the case of inadequate radiation shielding, proper

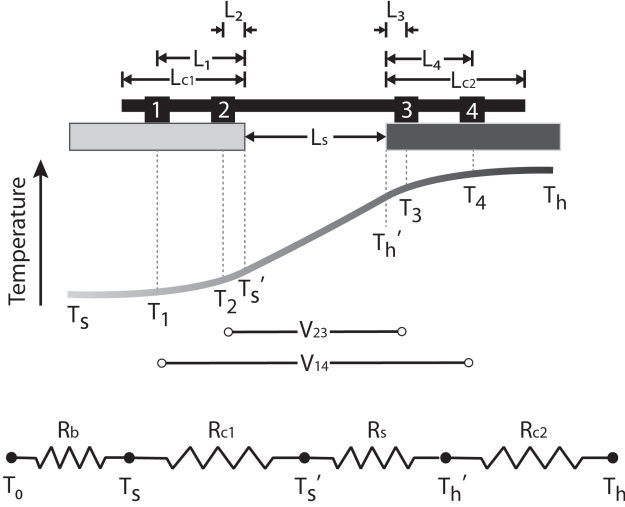


Figure 4: Four-probe thermoelectric measurement schematic with definitions of the length, temperatures, and thermal resistances used in the analysis.

radiation shielding is necessary to reduce the temperature difference between $T_s(I = 0)$ and T_0 during the temperature calibration of the sensing PRT. The use of one additional radiation shield thermally anchored to the sample stage can considerably reduce the temperature difference between the sensing PRT and the shield, as shown in Fig. 3(a).

The resistance of the heating PRT can be obtained from the measured $I - V$ curve as $R_h = V/I$. However, the obtained R_h becomes noisy when I approaches zero, as shown in Fig. 5(a). To address this issue, the differential resistance of the heating PRT can be calculated from the local slope of the $I - V$ curve as $R'_h = dV/dI$ [Fig. 5(b)]. However, the obtained $R'_h(I)$ and $R_h(I)$ are much noisier than the $R_s(I)$ measured with the use of a lock-in amplifier. It is possible to smooth the data by taking an analytic derivative of the third-order polynomial fit to the measured ΔV versus I [Fig. 5(c)], however, this provides no improvement in the actual measurement uncertainty. This problem can be overcome by coupling a small sinusoidal current $i_{1\omega} e^{i\omega\tau}$ to the large DC heating current I . The first-harmonic component of the voltage drop, $v_{1\omega} e^{i\omega\tau}$, across the heating serpentine can be measured with a lock-in amplifier, and used to obtain the AC resistance of the heating serpentine as $R_h = v_{1\omega}/i_{1\omega}$. In this case, the electrical heating in the heating serpentine becomes

$$Q_h = (I^2 + 2Ii_{1\omega} e^{i\omega\tau} + i_{1\omega}^2 e^{i2\omega\tau}) R_h(I) \quad (6)$$

Consequently, $\Delta T_h(I)$ contains a steady state component, a 1ω component, and a higher-order term. The higher-order term is negligible compared to the steady state and 1ω components, because of the relatively small applied sinusoidal current, giving $\Delta T_h(I) = a_0 I^2 + 2a_1 I i_{1\omega} e^{i\omega\tau}$. If ω is small compared to $1/\tau$, where τ is the thermal time constant of the device, $\Delta T_h(I)$ responds fully to the 1ω heating term just like it does to DC heating (i.e., $a_0 = a_1$). In the high-frequency limit, ω is much larger than $1/\tau$ so that $\Delta T_h(I)$ does not respond to the modulated heating (i.e., $a_1 \ll a_0$). The resulting temperature rise in the heating PRT for the two limiting cases is

$$\Delta T_h(I) \equiv \frac{\Delta R_h}{3dR_h/dT} \quad \text{for } \omega \ll 1/\tau \quad (7a)$$

$$\Delta T_h(I) \equiv \frac{\Delta R_h}{dR_h/dT} \quad \text{for } \omega \gg 1/\tau \quad (7b)$$

The factor of three difference is verified by the measured ΔR_h versus ω relation shown in Fig. 6. A detailed transfer function analysis of this 1ω measurement technique was given by Dames and Chen.⁴⁰ Because of the relatively large thermal time constant of the thermally isolated measurement device, the high-frequency limit can be readily achieved by using a frequency of > 1000 Hz which is well below the frequency range where electrical capacitive coupling can cause a noticeable phase lag between the measured $v_{1\omega}$ and $i_{1\omega}$.

Returning to the problem of accurately determining the temperature coefficient of resistance, Figure 7 shows the measured $R_s(I = 0)$ versus T_0 curve and the dR_s/dT of a PRT in the temperature range between

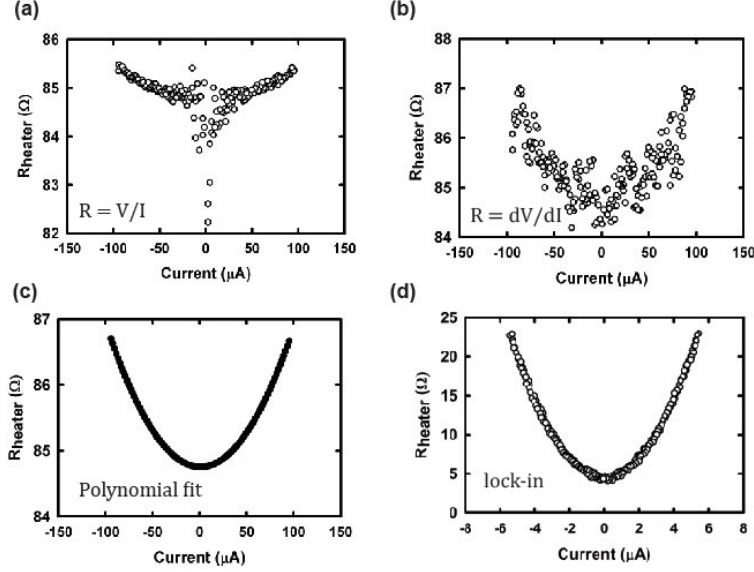


Figure 5: The resistance of the heating PRT as a function of the applied DC current determined by three methods: (a) the voltage rise, V , divided by the applied current, I ; (b) the five-point local derivative of dV/dI ; (c) the analytic derivative to the third-order polynomial fit of V versus I ; (d) the resistance of a different PRT measured with a lock-in amplifier by coupling a small AC current with a DC heating current.

4 and 700 K with two radiation shields. The resistivity is roughly linear at high temperatures, and falls approximately as T^5 at low temperatures. Depending on the nature of the impurities in the PRT, the resistance may increase again at very low temperature; the measured resistance in Fig. 7(a) clearly shows such dependence at < 50 K. The temperature coefficient of resistance, dR/dT , may be found from the local derivative to the R versus T curve, or alternatively, by fitting the measured resistance versus temperature to a linear fit or to the Bloch-Gruneisen (BG), T^5 law,

$$R(T) = R_0 + A \left(\frac{T}{\theta_D} \right) \int_0^{\theta_D} \frac{x^5 dx}{(e^x - 1)(1 - e^{-x})} \quad (8)$$

where R_0 is the residual resistance, θ_D is the Debye temperature, and A is a constant. Wingert et al.⁴¹ have used the BG relationship to fit the measured resistance of a PRT in the temperature range of 60 – 380 K with the fitting parameters A , R_0 , and θ_D , and found that a linear approximation to the resistance can lead to an 8% difference in the measured thermal conductivity at temperatures on the order of 100 K due to a peak in the temperature derivative at low temperature. Although the BG fit to the data shows a considerable improvement over a constant dR/dT value, the BG formula makes several key assumptions, which include neglecting the interactions of electrons with higher energy phonons and the assumption that electron states with the same wave vectors have nearly the same velocity. However, as the Fermi surface becomes increasingly complex, interband scattering becomes important. In addition, when the temperature is sufficiently high, the resistance can deviate from Eq. (8).⁴² In addition, Eq. (8) neglects any contribution from the Kondo effect, and thus cannot explain the resistivity below 10 K for certain materials with strong magnetic moments or a high concentration of magnetic impurities.⁴³ In this case, a polynomial fit to the data or the determination of the local derivative can be most accurate. Figure 7(b) shows the difference in the calculated dR/dT using a linear fit, a BG fit, and a local three-point derivative. For the linear fit and BG fit, only the data greater than 70 K is considered. Both the linear fit and BG fit fail at temperatures of < 100 K for this particular PRT. A more reasonable fit to the BG formula is possible by considering all data points, however, this gives unrealistic values for the fitting parameters, and therefore provides no clear advantage over using a simple polynomial fit.

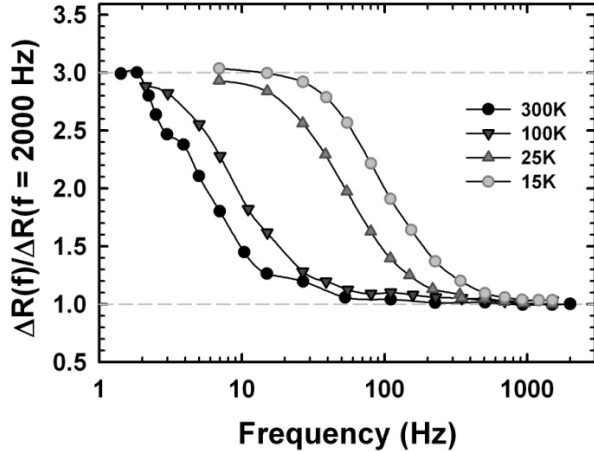


Figure 6: The measured resistance of the PRT as a function of the lock-in amplifier frequency, which shows a factor of three difference between the low and high frequency limits. Reproduced from Shi et al.²⁴ with permission from ASME. Copyright 2003.

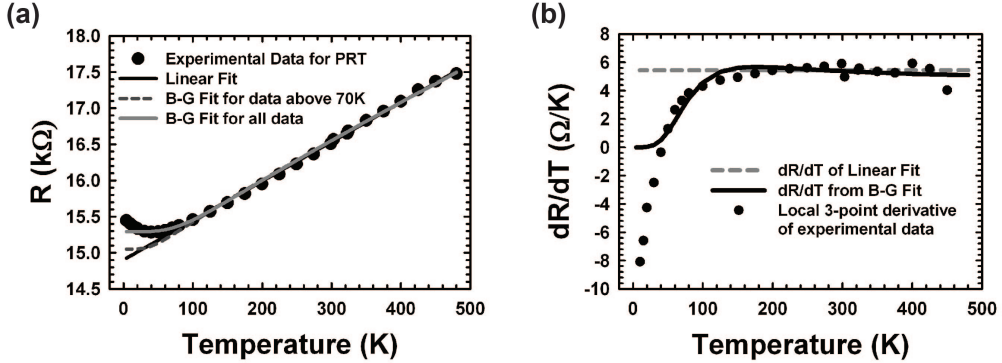


Figure 7: (a) Measured resistance (circles) as a function of temperature for a PRT of a suspended resistance thermometry device, with a linear and BG fit. (b) The temperature coefficient of resistance calculated with a local numerical derivative (circles) and the analytic derivative to the BG fit and linear fit.

3.3 Measurement Sensitivity

Figure 8 shows the electronic connections for measuring the resistance change of both PRTs with the use of two lock-in amplifiers. The noise in the measured resistance of the two PRTs was found to be dominated by a $\sim 40 \times 10^3$ K random fluctuation in the sensing membrane temperature when R_0 is near 300 K.²⁴ Because the thermal conductance of the supporting beam, $G_b \equiv 1/R_b$, is about 1×10^7 W/K and ΔT_h should be maintained at < 10 K for T_0 near 300 K, ΔT_s approaches the order of the random temperature fluctuation when the sample thermal conductance, $1/R_{total}$, is less than 0.5×10^9 W/K, which is equivalent to the thermal conductance of a 20 nm-diameter, 3 μm-long NW with a low thermal conductivity of 5 W/m K. For measuring this and other NWs of a smaller G_{total} , a large ΔT_h is required unless the random noise can be reduced. A recent work⁴¹ has reported the use of a Wheatstone bridge circuit to enhance the measurement sensitivity. In that work, the sensing PRT was connected in parallel with an additional serpentine PRT on an adjacent device on the same chip. The resistance ($R_{s,p}$) of this reference PRT is very close to that of the sensing PRT (R_s). In addition, two other resistors are paired with the measurement device outside the cryostat, including a high-precision resistor R_0 and a potentiometer R_p . The bridge is initially balanced by zeroing the measured differential voltage V_D by adjusting R_p . During the measurement, DC Joule heating of one membrane results in a temperature rise of the sensing membrane and resulting increase in R_s . With an AC voltage V_0 applied to the bridge circuit, the bridged voltage V_D is measured with a lock-in amplifier.

The resistance of the sensing membrane and two leads is then found from

$$R_s = R_0 \left(\frac{V_D}{V_0} + \frac{R_p}{R_p + R_{s,p}} \right)^{-1} - R_0 \quad (9)$$

The bridge circuit takes advantage of the fact that fluctuations in the substrate temperature will affect both R_s and $R_{s,p}$ equally, generating a net zero change in the bridge voltage V_D . The sample conductance can then be found in a similar manner as described previously from the sensing and heating membrane resistance. Because the effect of the substrate temperature fluctuation in the sensing PRT is canceled by a similar fluctuation in the reference PRT, the process increases the G_{total} sensitivity to roughly 1×10^{11} W/K, when a large voltage is applied to the bridge circuit and the measurement time constant is long. The bridge circuit also yields an additional benefit because only the change in the voltage drop along the sensing PRT is measured by the lock-in amplifier, so that the resolution of the lock-in amplifier can be fully utilized.

However, even without a NW bridging the two membranes, a background thermal conductance (G_{bg}) as high as 0.3×10^9 W/K at 300 K can be measured between the two membranes,³⁰ because of residual gas molecules, thermal radiation, and heating of the substrate. In the case that G_{total} is comparable to or smaller than G_{bg} , the measurement uncertainty can be appreciable. Hence, this method cannot be used to measure a sample with G_{total} much smaller than about 0.3×10^{10} W/K.

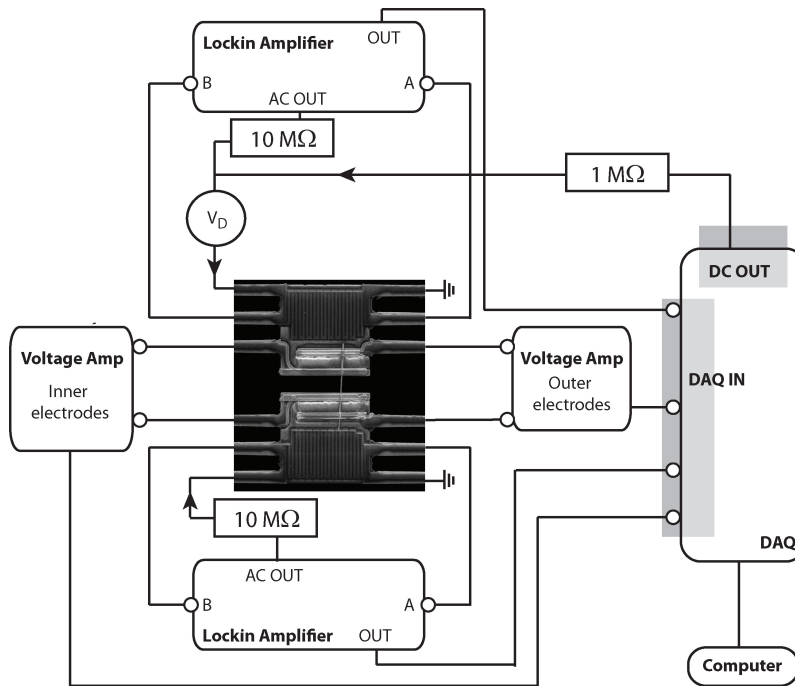


Figure 8: Schematic of the measurement setup for four-probe thermoelectric property measurement of suspended nanostructures.

3.4 Contact Resistance and Four-Probe Thermoelectric Measurement Procedure

According to the thermal resistance circuit in Fig. 4, the as-measured two-probe thermal resistance of the sample includes a contribution from the contact resistance between the NW and the two membranes. In an attempt to minimize the contact thermal resistance, Hippalgaokar et al.⁴⁴ have patterned an array of Si NWs from a thin Si membrane, with the PRT/SiN_x membrane deposited directly onto the supporting substrate on either ends of the nanowires. By measuring NW arrays of a similar cross section and different lengths, they determined that the intrinsic thermal resistance of the suspended NW array was much larger than the constriction thermal resistance at the nanowires ends, and the interface thermal resistance between the SiN_x membrane and the Si pad. Length-dependent thermal resistance has also been employed to determine the

contact thermal resistance between carbon nanotubes and the suspended membranes.⁴⁵ In comparison, for a NW assembled by drop casting between two suspended membranes, the contact thermal resistance between the NW and the membrane can vary greatly depending on the material, contact area, and the interface adhesion energy.

To resolve the issue of the unknown contact resistance, Mavrokefalos et al.²⁶ have devised a four-probe thermoelectric measurement procedure to obtain the contact thermal resistances at the two ends of a NW sample and thus determine the intrinsic thermal conductivity, Seebeck coefficient, and electrical conductivity of the suspended NW. In this method, two thermovoltages were measured between the two outer electrical contacts and the two inner electrical contacts to the NW, $V_{14} = S(T_1 - T_4)$ and $V_{23} = S(T_2 - T_3)$ (Fig. 4), where S is the Seebeck coefficient of the NW and is assumed to be uniform along the entire NW and much larger than that of the metal electrodes.

Figure 4 also shows a representative temperature distribution across the NW, considering the nanowires to be a fin of constant cross section. The temperature across the suspended segment is linear when the radiation loss from the NW is negligible. Because of heat transfer through the NW-membrane contact, the temperature distribution along the supported NW varies approximately exponentially. The thermal contact resistance can then be calculated from the fin resistance formula,

$$R_{c,i} = \frac{1}{\kappa A m \tanh mL_{c,i}} \quad i = 1, 2 \quad (10)$$

where κ is the thermal conductivity, A is the cross-sectional area of the suspended NW, $L_{c,i}$ is the length of the NW in contact with the membrane as defined in Fig. 4, and $m = \sqrt{hb/\kappa A}$, where h is the thermal contact conductance per unit area and b is the contact width between the NW and membrane. From the thermal resistance circuit in Fig. 4, together with the definition of the sample resistance, $R_S = L_s/\kappa A$, and the fin temperature profile, the dimensionless temperature is related to the two measured thermovoltages according to

$$\gamma \equiv \frac{\gamma_{14}}{\gamma_{23}} = \frac{T_1 - T_4}{T_2 - T_3} = \frac{V_{14}}{V_{23}} \quad (11)$$

where

$$\begin{aligned} \gamma_{ij} \equiv \frac{T_i - T_j}{T'_h - T'_s} &= 1 + \frac{1 - \cosh m(L_{c,1} - L_i)/\cosh mL_{c,1}}{L_s m \tanh mL_{c,1}} \\ &\quad + \frac{1 - \cosh m(L_{c,2} - L_i)/\cosh mL_{c,2}}{L_s m \tanh mL_{c,2}} \end{aligned} \quad (12)$$

The intrinsic thermal resistance and Seebeck coefficient of the NW can be found from

$$S = \frac{\alpha V_{23}}{\gamma_{23}(T_h - T_s)}; \alpha = \frac{T_h - T_s}{T'_h - T'_s} = 1 + \frac{1}{L_s m} \left[\frac{1}{\tanh mL_{c,1}} + \frac{1}{\tanh mL_{c,2}} \right] \quad (13)$$

$$R_s = \frac{R_{total}}{\alpha} \quad (14)$$

For CrSi₂ NWs, Zhou et al.²⁷ have found the contact resistance accounts for 10% of the measured R_{total} . In comparison, Mavrokefalos et al.²⁶ have found this contribution to be as high as 15-20% for InAs thin films.

In addition to the thermal conductivity and Seebeck coefficient, the four-probe electrical conductivity can also be measured on the suspended resistance thermometer device, allowing for characterization of all three axial thermoelectric properties on the same NW. The electrical current used for the four-probe $I - V$ measurement of the NW can result in Peltier cooling and heating at the two contacts, and result in a temperature difference between the two membranes. The temperature difference can introduce a thermovoltage component in the measured four-probe voltage. This thermovoltage component can be determined from the previously obtained S of the NW as well as the temperatures of the two membranes measured with the use of the two PRTs.

This four-probe thermoelectric measurement method is limited to electrically conducting NW or nanofilm samples with a sufficiently large Seebeck coefficient that is uniform along the entire length. However, for atomically thin NWs, nanotubes, and films such as graphene, the Seebeck coefficient depends sensitively on the surface charges, and may be rather different between the suspended segment and supported segment of the sample. Hence, this method has not been used to obtain the contact thermal resistance to graphene or carbon nanotubes.

4 T-Junction Sensor for Thermal Conductance Measurement

Fujii et al.⁴⁶ reported a T-junction nanofilm sensor for measuring the thermal conductivity of a multiwalled carbon nanotubes (CNTs) inside an SEM or TEM column, which can be used to characterize the crystal structure and cross section of the measured nanostructure sample. In this measurement, one end of the CNT was mounted, with the assistance of focused electron beam irradiation, to a heat sink at one end and to the center of a patterned suspended Pt nanofilm sensor at the other. Figure 9 shows a variation of this measurement setup reported by Dames et al.,⁴⁷ in which a scanning tunneling microscope (STM) tip was used as the heat sink on one end of the CNT, which could be manipulated to bring the CNT into contact with the electrically heated nanofilm sensor. The average temperature rise of the electrically heated nanofilm sensor was determined from the measured electrical resistance before and after the CNT made contact. For the case when a CNT with thermal resistance R_{CNT} is brought into contact with the midpoint, $x = 0$, of the hotwire sensor, the average temperature rise of the sensor can be found from the heat conduction equation as

$$\theta = \frac{1}{12}QR_{HW} \left[1 - \frac{3}{4}(1 + \gamma^{-1})^{-1} \right] \quad (15)$$

where Q is the Joule heat generation in the hotwire, $\gamma = R_{HW}/4R_{CNT}$, $R_{HW} = L_{HW}/\kappa_{HW}A_{HW}$, and L_{HW} , A_{HW} , and κ_{HW} are the length, cross section, and thermal conductivity of the hotwire. The derivative of Eq. (15) with respect to γ reaches a maximum when γ approaches unity, and zero at sufficiently low and high values of γ . Hence, the maximum measurement sensitivity is obtained when R_{HW} is designed to be close to $4R_{CNT}$. In the measurement, R_{HW} can be obtained based on Eq. (15) from a separate measurement made before the CNT made contact to the hotwire, where $\gamma = 0$.

This analysis assumes that the CNT makes contact at exactly the midpoint of the sensor. In the case that the sample is offset slightly from $x = 0$, a correction factor is needed. Dames et al.⁴⁷ have shown that this fractional error is approximately $8(l/L_{HW})^2$ and is $< 10\%$ as long as the offset, ℓ , is < 0.112 times the length of the hotwire. In addition, radiation loss is not accounted for in this conduction analysis. For both the hotwire and the nanotube, the ratio of radiative heat transfer to conductive heat transfer scales as the product of the fin parameter (β) and length, $\beta L = h_{rad}P/\kappa AL$, where h_{rad} is the heat transfer coefficient for radiation and is approximately equal to $h_{rad} = 4\epsilon_{rad}\sigma T^3$, and ϵ , κ , A , and P are the emissivity, thermal conductivity, cross section, and perimeter of the nanotube or hotwire. Dames et al.⁴⁷ derived the relative error caused by neglecting the radiation loss to be approximately $(\beta L)^2/10$. This relative error can increase

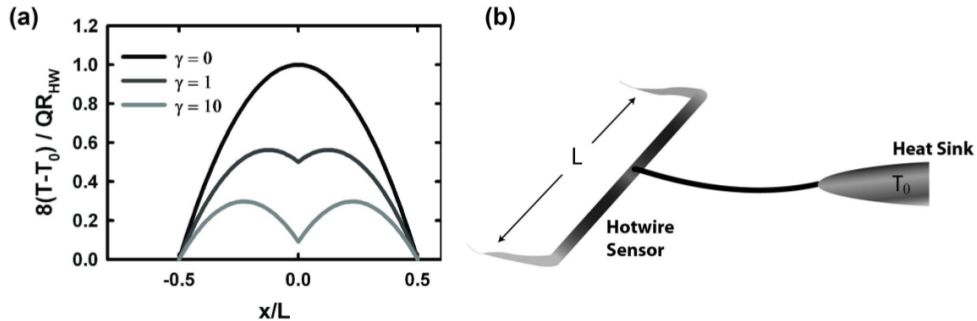


Figure 9: (a) Temperature profile along the length of the hotwire probe from Dames et al.⁴⁷ for varying ratios, γ , of the hotwire and sample thermal resistance. (b) A schematic of the measurement setup for the same work. Reproduced with permission from Dames et al.⁴⁷ by American Institute of Physics. Copyright (2007).

from $< 0.48\%$ for a $3 \mu\text{m}$ -diameter, 2 mm-long Pt hotwire, to up to 32% for a $0.5 \mu\text{m}$ -diameter, 5 mm-long Pt hotwire. Although the radiation loss from the hotwire can be reduced by increasing its diameter and thermal conductivity and reducing its length, doing so would reduce γ , and hence the sensitivity in the measurement of R_{CNT} .

5 Direct Thermal Conductance Measurement with Bimaterial Cantilever Sensor

Recently, Shen et al.⁴⁸ have reported a method based on a Si₃N₄/Au bimaterial cantilever thermal sensor to measure the thermal conductivity of stretched polyethylene nanofibers. In their measurement, the polyethylene nanofibers were drawn directly from a polymer gel with the use of the bimaterial cantilever, with a draw ratio between 60 and 800. The fiber was cut at a distance of $\sim 300 \mu\text{m}$ from the cantilever. The cut end of the fiber was then attached to a microthermocouple that could be externally heated. Because of the thermal expansion mismatch between the two constituent materials of the cantilever, the heat flow (Q_C) from the fiber into the cantilever tip can be obtained from the cantilever tip deflection, which is determined from the position of the reflection of a laser beam focused on the cantilever.

The thermal measurement was conducted in vacuum to eliminate heat loss to the surrounding gas molecules. The measurement method falls in the same category of comparative measurements as that based on the suspended Pt serpentine resistance thermometer devices discussed in a previous section. According to the thermal circuit of Fig. 10, with a fixed laser power (Q_L) absorbed by the cantilever and varying thermocouple temperature (T_A) at one end of the fiber,

$$R_{NF} = R_{cantilever} \frac{\Delta T_A - \Delta T_L}{\Delta T_L} \quad (16)$$

where R_{NF} and $R_{cantilever}$ are the thermal resistance of the nanofiber and the cantilever sensor, and ΔT_A and ΔT_L are the external changes in thermocouple and cantilever tip temperature (T_L) when Q_L is kept constant. In principle, $R_{cantilever}$ can be obtained from the change in the measured T_L when Q_L is varied, prior to the attachment of the nanofiber to the cantilever. However, the temperature is nonuniform in the cantilever during the thermal measurement of the nanofiber, so that it is difficult to calibrate the cantilever deflection versus a uniform cantilever temperature and use the calibration result to determine ΔT_C during thermal measurement of the nanofiber. Instead, Q_C is calibrated against the measured cantilever tip deflection signal. Ideally, this calibration should be done in vacuum before the nanofiber is attached to the cantilever, so that Q_C equals the absorbed laser power (Q_L) of the cantilever. Nevertheless, because R_{NF} is three orders of magnitude larger than $R_{cantilever}$, the heat loss through the nanofiber attached to the cantilever can be neglected compared to Q_C , so that the calibration can be performed with the nanofiber attached to the

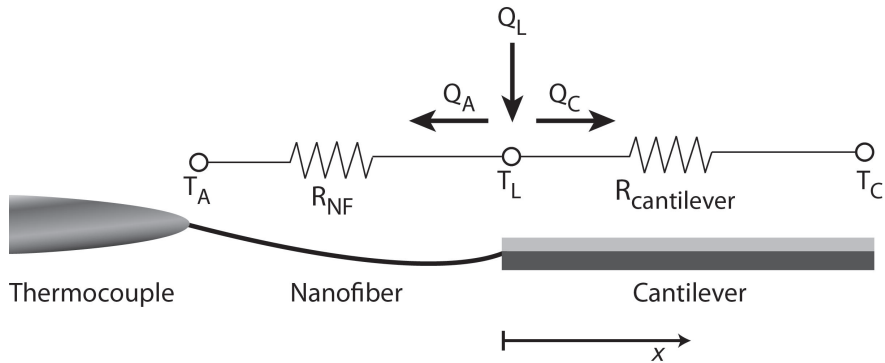


Figure 10: (a) Thermal circuit for the measurement of a polyethylene nanofiber using a bilayer cantilever and a heated thermocouple. Q_L refers to the power absorbed by the incident laser, and T_L is the temperature of the cantilever at the laser spot, R_{NF} and $R_{cantilever}$ are the corresponding thermal resistances, and T_A and T_C are the temperatures of the thermocouple and cantilever base, respectively. Reproduced from Shen et al.⁴⁸ with permission from Macmillan Publishers Ltd: Nature. Copyright 2010.

cantilever. Their calibration yielded the ratio

$$\alpha_1 = \frac{\Delta Q_{L_{\Delta P}}}{\Delta B_{\Delta P}} \approx \frac{Q_{C_{\Delta P}}}{\Delta B_{\Delta P}} \quad (17)$$

where $\Delta Q_{L_{\Delta P}}$, $\Delta Q_{C_{\Delta P}}$, and $\Delta B_{\Delta P}$ are the changes in Q_L , Q_C , and the cantilever deflection signal, respectively, when the incident laser power (P) is varied and the thermocouple temperature T_A is held constant.

After calibration, R_{NF} was determined by varying T_A while maintaining constant Q_L . The corresponding change in Q_C can be obtained as $\Delta Q_{C_{\Delta T_A}} = \alpha_1 \Delta B_{\Delta T_A}$, where $\Delta B_{\Delta T_A}$ is the corresponding change in the measured cantilever deflection signal. Hence,

$$R_{NF} = \frac{\Delta T_A - \Delta T_{L_{\Delta T_A}}}{\Delta Q_{C_{\Delta T_A}}} \approx \frac{\Delta T_A}{\Delta Q_{C_{\Delta T_A}}} \quad (18)$$

where $\Delta T_{L_{\Delta T_A}}$ is the corresponding change in the cantilever tip temperature, and is about three orders of magnitude smaller than ΔT_A because R_{NF} is three orders of magnitude larger than $R_{cantilever}$.

Because the $\sim 300 \mu\text{m}$ length of the nanofiber is three orders of magnitude larger than its diameter of $\sim 130 \text{ nm}$, it is necessary to evaluate the radiation loss from its circumference in addition to heat conduction in the nanofiber. The nanofiber can be treated as a radiative fin, with its thermal resistance related to the emissivity (ϵ) and thermal conductivity (κ) as

$$R_{NF} = \frac{\sinh \beta L}{\sqrt{\pi^2 \epsilon \sigma \kappa T^3 D^3}} \quad (19)$$

where $\beta = \sqrt{16\epsilon\sigma T^3/D\kappa}$, T is the average temperature of the system, and κ , D , and L are the thermal conductivity, diameter, and length of the nanofiber, respectively. For $\beta \ll 1$, Eq. (18) is reduced to the case of pure conduction, $R_{NF} = L/\kappa A$, which was used to obtain a κ value of $\sim 104 \text{ W m}^{-1}\text{K}^{-1}$. For the corresponding R_{NF} value and an emissivity $\epsilon = 0.1$, Eq. (18) would yield a κ value of $104.4 \text{ W m}^{-1}\text{K}^{-1}$, just slightly higher than that determined from neglecting radiation loss. The difference is negligible because of a small βL value of 0.12.

A unique advantage of this measurement was that the bimaterial sensor was used for both drawing the nanofiber and for measuring its thermal property. However, it is of interest to evaluate the temperature and heat flow rate measurement sensitivities of the bimaterial cantilever thermal sensor, and compare them with those achievable by resistance thermometry. Based on the measurement data reported by Shen et al.,⁴⁸ the cantilever sensor is sensitive to about 3 K temperature change of T_A , which is equivalent to about 3×10^3 K change in T_L . The measurement sensitivity in Q_C is thus on the order of 30 nW/K based on their reported $R_{cantilever}$ value on the order of 10^5 K/W, and can potentially be improved to about 0.3 nW/K if $R_{cantilever}$ is increased to the level of 10^7 K/W found for the thermal resistance of the supporting beams on suspended resistance thermometer devices.²⁴ In addition, one source of error for this optical measurement is the uncertainty in the absorbed laser power Q_L , which Shen et al.⁴⁸ determined to be as small as a $\sim 9\%$ of the incident power and is found from subtracting the reflected and strayed beam intensity from the incident intensity. The diffusely scattered laser power was thought to be small, and neglected in their measurement. In comparison, it is feasible to determine the heating in the cantilever rather conveniently and accurately if the heating is provided by electrical heating of a doped Si or Pt-C resistor fabricated at the end of a cantilever.^{49,50} This type of resistance thermometer can achieve 3 mK temperature sensitivity with the use of lock-in detection combined with a Wheatstone bridge. The resistance of the thermometer can also be calibrated readily as a function of the cantilever temperature, and the method is free of the complication caused by thermal drifting of the laser beam as well as cantilever deflection caused by mechanical strain applied by the nanofiber. This suggests that in addition to bimaterial cantilevers, resistance thermometer cantilever sensors can also potentially provide an attractive method for thermal measurements. However, the fabrication of the resistance thermometer cantilever sensors indeed requires additional steps of fabrication of the doped Si or Pt-C resistance thermometer sensor at the end of the cantilever.

6 Thermal Diffusivity Measurements with Doped Si Cantilever Resistance Thermometer Sensors

Resistance thermometer cantilever sensors have been explored for thermal diffusivity measurements of polymer fibers by Demko et al.⁴⁹ The thermal sensor is a Si cantilever with two heavily doped beams connected by a lightly doped Si region that acts as the resistance thermometer (see Fig. 11). The thermal measurement was conducted inside a SEM chamber that was equipped with a nanomanipulator. During the measurement,

a nanofiber was suspended between the end of the Si cantilever and an aluminum support. After a Joule heated micromanipulator probe was brought into contact with a point along the suspended segment of the nanofiber, the time evolution of electrical resistance of the Si thermometer was monitored by recording the voltage output from a Wheatstone bridge circuit. If the thermal interface resistance at the two contacts to the nanofiber is ignored, the fiber-probe contact point will maintain a constant temperature of the heated probe. Under this condition, a solution to the junction temperature between the nanofiber and the Si cantilever can be found in Carslaw and Jaegers⁵¹ for the case of two finite slabs in thermal contact. The solution can be simplified for low-thermal conductivity and low-diffusivity samples that satisfy the following conditions,

$$\frac{\kappa_s A_s}{\kappa_f A_f} \sqrt{\frac{\alpha_f}{\alpha_s}} = \frac{A_s}{A_f} \sqrt{\frac{\kappa_s \rho_s C_s}{\kappa_f \rho_f C_f}} \gg 1 \quad \text{and} \quad \sqrt{\frac{\alpha_f}{\alpha_s}} \ll \sqrt{\frac{\ell_f}{\ell_s}} \quad (20)$$

where κ , α , ρ , C , A , and ℓ refer to the thermal conductivity, diffusivity, density, heat capacity, cross section, and length of the sensor and fiber, denoted with the subscript s and f , respectively. In the simplified solution, the normalized temperature at the fiber-cantilever junction located at $x = 0$ is given as

$$T^*(t) = \frac{\Delta T|_{x=0}}{\Delta T_m} \frac{\kappa_s A_s \ell_f}{\kappa_f A_f \ell_s} = 1 + 2 \sum_{n=1}^{\infty} (-1)^n e^{-(\alpha_f n^2 \pi^2 t / \ell_f^2)} \quad (21)$$

where $\Delta T|_{x=0}$ and ΔT_m refer to the temperature rise at the fiber-cantilever interface and that of the micromanipulator bought in contact at $x = \ell_f$. The measured time evolution of the sensor signal was fit to the functional form of Eq. (20) to extract the thermal diffusivity of the sample.

For this thermal flash measurement of diffusivity to be sensitive and accurate, $\Delta T|_{x=0}$ needs to be large compared to the temperature sensitivity on the order 10^{-3} K of the resistance thermometer sensor. For ΔT_m of order 10 K, the ratio between the thermal resistance of the fiber and that of the cantilever sensor, $R_f/R_s = \kappa_s A_s \ell_f / \kappa_f A_f \ell_s$, needs to be less than the order of 10^4 . In addition, because the lightly doped resistance thermometer sensor has a finite size, l_{RT} , the thermal time constant of the sensor needs to be considerably smaller than that of the fiber, that is, $l_{RT}^2 / \alpha_s \ll \ell_f^2 / \alpha_f$, in order to establish sufficient transient response of the sensor. In the work of Demko et al.,⁴⁹ the samples were glass fibers and polyimide fibers with considerably lower thermal diffusivity than the Si sensor. For extending this method to a high-thermal diffusivity carbon nanotube of a finite length, the size of the resistance thermometer may need to be reduced to be considerably smaller than the length of the nanotube sample.

The above solutions are based on the absence of contact thermal resistance at the two ends of the nanofiber. With the presence of a contact thermal resistance ($R_{f,c}$), the fiber temperature at the fiber-cantilever contact ($T_{f,c}$) varies with time so that the above solution is not strictly applicable. However, when the thermal penetration depth increases with time to be larger than $R_{f,c} A \kappa$, $T_{f,c}$ approaches a constant equal to the probe temperature. Hence, the above solution can still be used to fit the time variation of the sensor signal after the initial response and extract the thermal diffusivity, although both the time evolution and amplitude of the initial sensor response depend on the contact thermal resistance. Compared to a steady state measurement of the thermal conductivity, the error caused by the contact thermal resistance is small but still present in the thermal flash measurement of the thermal diffusivity. However, accurate knowledge of the density and heat capacity is necessary to convert the measured thermal diffusivity to thermal conductivity.

7 Three Omega Techniques

The 3ω technique for NW thermal conductivity measurement is a further development of the celebrated method reported by Cahill⁵² for thin film measurements. For NW measurements, the NW is suspended with four electrical contacts to the NW, as illustrated in Fig. 12. A sinusoidal current at 1ω angular frequency is supplied to the NW sample, and induces a temperature modulation at the 2ω frequency. The 2ω temperature fluctuation in turn generates a 3ω component in the voltage drop measured across the suspended NW. Measured with a lock-in amplifier, the rms amplitude of the 3ω voltage component is given by

$$V_{3\omega} = \frac{4I^3 LR(dR/dT)}{\pi^4 \kappa A \sqrt{1 + (2\tau\omega)^2}} \quad (22)$$

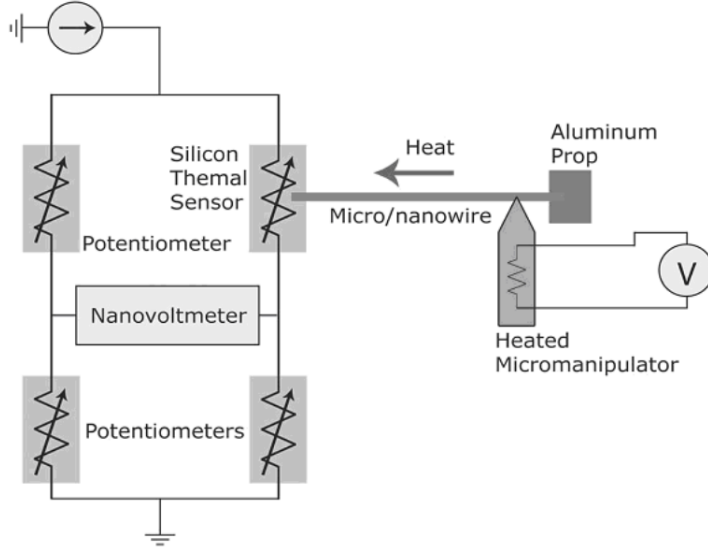


Figure 11: Schematic of the setup by Demko et al.⁴⁹ to measure the diffusivity of polyimide nanofibers. Reproduced from Demko et al.⁴⁹ with permission from American Institute of Physics. Copyright 2009.

where the thermal time constant $\tau = L^2/\pi^2\alpha$, and L , α , and R are the length between the voltage leads, thermal diffusivity, and electrical resistance of the NW sample. I is the rms amplitude of the time-dependent current, $I_0 \sin \omega t$. The experimental results can be fit to Eq. (21) to extract the thermal conductivity and thermal time constant. The specific heat can then be found from

$$C_p = \frac{\pi^2 \tau \kappa}{\rho L^2} \quad (23)$$

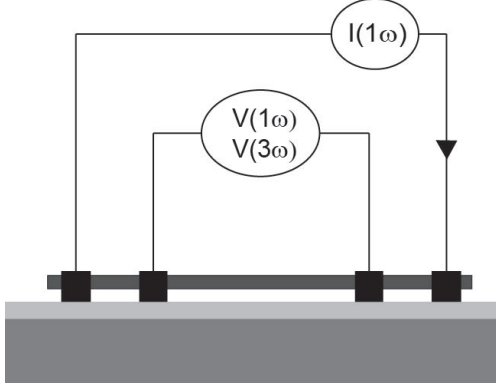


Figure 12: Schematic of the 3ω measurement of thermal conductivity and diffusivity of a suspended nanowire.

The thermal conductivity is often measured in the low frequency limit where the amplitude in the temperature fluctuation is a maximum, and where the frequency dependent term in Eq. (21) drops out. This is particularly important for the case of a long sample, where a low frequency is needed so that the temperature modulation is larger than the measurement sensitivity. Conversely, to obtain the specific heat, the measurement needs to be performed at sufficiently high frequency compared to $1/\tau$,⁵³ so that $V_{3\omega}$ shows a clear frequency dependence. For an individual carbon nanotube of a length of several micrometers and a high thermal diffusivity, the frequency needs to be as high as 10 MHz in order to be able to measure the specific heat. Measurements at such a high frequency can be prone to errors caused by electrical capacitive coupling and other limitations in electronics.

The 3ω method has been used to measure the thermal conductivity and specific heat of a number of conducting NWs and CNTs. Among the early 3ω measurements is the work reported by Yi et al.⁵⁴ on the

thermal conductivity and specific heat measurement of 1-2 mm long multiwalled carbon nanotube (MWCNT) bundles suspended over an etched trench. The 3ω method has also been used for investigating thermal transport in Pt NWs at cryogenic temperatures,⁵³ the Lorenz number in Ni NWs at low temperature,⁵⁵ the study of phonon-surface scattering in metal-coated Si NWs,⁵⁶ the effect of twinned boundaries on the thermal conductivity of InAs NWs below 6 K,⁵⁷ and individual defective CNTs.⁵⁸

A key advantage of using the self-heating 3ω method is that the transient measurement gives not only the thermal conductivity, but also the specific heat and diffusivity. In addition, because the NW acts as a simple heater and sensor, the device fabrication is relatively simple. Compared to steady state self-electrical heating and resistance thermometry methods, the 3ω method allows for sensitive frequency domain measurement of the induced temperature rise in the NW sample. In addition to the 3ω method, the 1ω and 2ω frequency components of the voltage drop can be measured when there is a DC offset in the applied modulated heating current. One example is the 1ω measurement of the DC temperature rise in the heating Pt serpentine of the resistance thermometer device of a large thermal time constant.²⁴ A detailed analysis of the 1ω , 2ω , and 3ω detection methods is given by Dames and Chen.⁴⁰

However, these self-electrical heating methods require that the NWs have a nearly constant temperature coefficient of resistance (TCR) in the measurement temperature range. The presence of a temperature-dependent TCR requires a rather cumbersome analysis. Moreover, one requirement of the validity of the self-heating methods is that the nonlinearity in the $I - V$ behavior should be due entirely to the change in lattice temperature, and that the electrons are indeed in thermal equilibrium with the lattice. For example, in the case of a short suspended CNT sample with scattering mean free path between optical or acoustic phonons comparable to or longer than the suspended length, the local electron or optical phonon temperature can be considerably higher than the acoustic phonon temperature. In this regime of highly nonequilibrium transport, it is not possible to convert the change in the measured electrical resistance to a calibrated temperature rise in the sample.

8 Transient Electrothermal Techniques

Besides modulated and DC electrical self-heating, pulse electrical self-heating of the NW sample can be employed for measuring the thermal conductivity and diffusivity of a suspended NW sample, with some potential advantages and disadvantages. Guo et al.⁵⁹ have demonstrated this method with Pt wires, single-walled carbon nanotube (SWCNT) bundles, and Au-coated polyester fibers. In one of the implementations, the NW is suspended across two copper electrodes, and a step function current is applied from time $t = 0$ to heat the sample.⁵⁹ The electrical resistance of the wire was measured to determine the average temperature rise in the suspended wire. With the radiation loss ignored, the normalized average temperature rise of the wire is given as

$$T^*(t) = \frac{T(t) - T_0}{T(t \rightarrow \infty) - T_0} = \frac{96}{\pi^4} \sum_{m=1}^{\infty} \frac{1 - \exp(-[(2m-1)^2 \pi^2 \alpha t / L^2])}{(2m-1)^4} \quad (24)$$

where the steady state temperature $T(t \rightarrow \infty) = T_0 + q_0 L^2 / 12\kappa$, and q_0 is the heat dissipation per unit volume in the nanowire, L its length, and κ is the thermal conductivity. The thermal conductivity can be obtained from the steady state average temperature rise, $\Delta T(t \rightarrow \infty)$.

At short times after the heating begins, when the heat transfer to the two ends of the NW is sufficiently small, the temperature change in the wire depends linearly on time as, $\Delta T = \Delta t q_0 / \rho C_p$, which agrees with the limiting case of Eq. (23), that is, $T^* = 12\Delta t \alpha / L^2$. Hence, the diffusivity can be conveniently obtained from a linear fitting of the initial time response of T^* . Alternatively, the entire T^* versus t response can be fitted with Eq. (23) to obtain the thermal diffusivity. Besides a step increase in the heating current, similar solutions can be found for a step decrease of the heating current.^{60,62}

In addition, it has been suggested by these works that the signal-to-noise ratio in pulsed electrical heating is greater than that of the 3ω method, and has the advantage of a shorter measurement time.⁶² However, the pulsed heating/sensing methods described are suitable only for materials with relatively low diffusivity and/or long lengths. For example, carbon nanotubes, with diffusivity on the order of $2 \times 10^4 \text{ m}^2/\text{s}$ and lengths on the order of $10 \mu\text{m}$, have a thermal time constant, L^2/α , of $2 \mu\text{s}$. In this case, the time scale of the transient temperature response is on the same order as the rise time of most current sources, i.e., $\sim 2 \mu\text{s}$,⁶² making it difficult to differentiate the contribution from the rise in electric signal from the rise in sample temperature.

To address this issue, periodically modulated nanosecond laser pulses have been employed to heat the sample.⁶² Under the assumption of a square pulse of uniform intensity along the length of the suspended NW, the normalized average temperature rise in the suspended NW was obtained as

$$T^* = \frac{T(t) - T_{min}}{T_{max} - T_{min}} = \frac{8}{\pi^2} \sum_{m=1}^{\infty} \frac{\exp(-[(2m-1)^2 \pi^2 \alpha t / L^2])}{(2m-1)^2} \quad (25)$$

where T_{min} and T_{max} are the minimum and maximum temperatures of the sample during pulsed heating. The average temperature rise in the suspended NW was determined from the electrical resistance of the sample measured with the use of a small DC current. By fitting the measurement data with Eq. (24), this method has been employed to obtain the thermal diffusivity of MWCNT bundles, Pt wires, and carbon fibers. However, without knowledge of the optical absorption of the sample, the measurement does not yield the thermal conductivity directly.

9 Raman Thermometry-based Measurements

Raman spectroscopy has been explored to probe thermal transport in CNTs,⁶³⁶⁵ graphene,⁶⁶⁶⁸ and GaAs NWs.⁶⁹ The sample temperature can be determined from the Raman spectrum in one of two ways. First, the Stokes to anti-Stokes intensity ratio can provide the optical phonon temperature within the laser spot. However, the ratio depends only on the zone center or zone boundary optical phonon populations, and the temperature therefore corresponds to only the temperature of these Raman active modes. Moreover, the anti-Stokes peak is observable only after the sample temperature is heated to a high temperature, and as high as 600 K for the case of graphene. On the other hand, as the temperature of the sample is increased, the Raman peaks become broadened and shifted due to increased lattice anharmonicity. The shift in either the 2D band or G band peak of the Raman spectrum has been used to probe the temperature of graphene. However, the temperature sensitivity is typically only on the order of 20-50 K.⁶⁵ In addition, charged impurities and strain can contribute to the Raman peak shift. Therefore, it is important that the strain and impurity scattering remain essentially constant throughout the measured temperature range, to ensure the peak shift can be attributable to temperature change alone. A further complication in Raman-based thermometry is the possible presence of nonequilibrium phonon transport among the acoustic modes and the Raman-excited optical modes. If acoustic modes, with very long mean free path, do not participate in the relaxation of the absorbed photons and hot electrons in the optically heated or electrically biased sample, or do not interact effectively with the optically excited Raman modes, they will be at a lower temperature than the optical phonon or electron populations. This is particularly important for very short CNTs when the optical phonon transport is quasi-ballistic.

Despite these experimental complications, Raman measurements on graphene, CNTs, and semiconducting NWs have yielded useful insight into phonon transport in nanostructures. Hsu et al.⁶⁵ have studied the heat transfer in suspended SWCNTs by recording the shift in the G peak as the laser spot was scanned along the nanotube suspended across a trench. Based on a separate calibration, the measured G peak shift was converted to the local temperature rise in the CNT. The obtained temperature profile suggested diffusive phonon transport in the defective CNT sample can be fit to the parabolic temperature profile with a curvature given by $Q/\kappa AL$, where Q is the optical heating rate absorbed by the nanotube, κ , A , and L are the thermal conductivity, cross section, and length of the nanotube. Because Q is unknown, this measurement can provide only the ratio of contact resistance to sample resistance of the suspended CNT. The ratio ranged from 0.02 to as high as 17. In another work on GaAs NWs, Soini et al.⁶⁹ used an ab initio finite difference simulation to extract the Q term, allowing for the calculation of the thermal conductivity from the temperature profile of the NW.

In order to experimentally determine the optical absorption in a CNT, Hsu et al.⁷⁰ focused a Raman laser beam onto a ~ 400 nm segment of a ~ 10 μm -long SWCNT bundle suspended between two suspended microscale Pt resistance thermometers, and measured the temperature rises (ΔT_1 and ΔT_2) at two thermometers. The laser power absorbed by the nanotube was taken to be the $Q = (\Delta T_1 + \Delta T_2)/R_b$, where R_b is the thermal resistance of the supporting beams for each thermometer. With the contact thermal resistance ignored, the temperature of the CNT at the laser spot was determined from the red shift of the G band, and used together with Q to obtain the thermal conductivity.

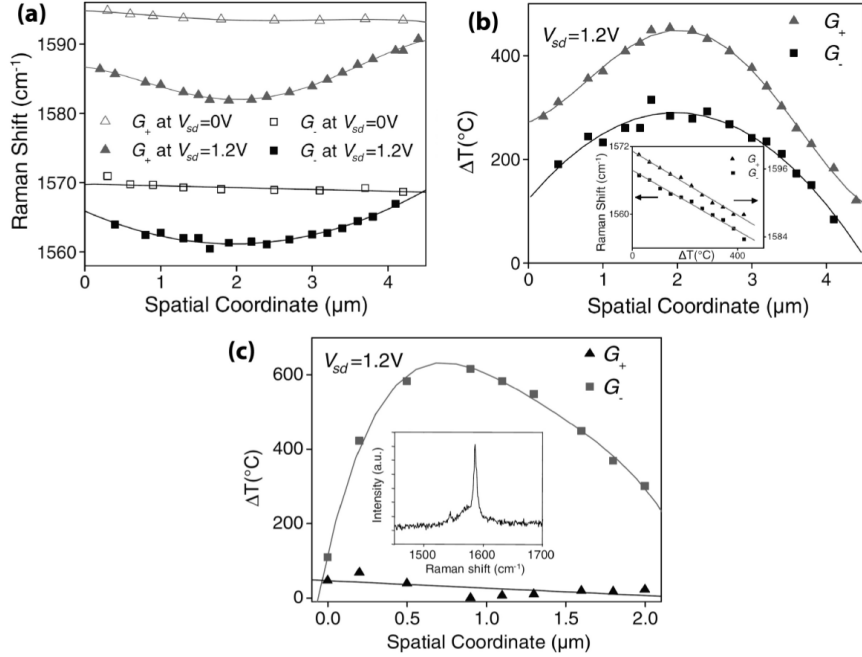


Figure 13: (a) Raman shift of a 5 μm -length suspended CNT and (b) corresponding temperature profile for the G and G^+ phonon modes. (c) Temperature profile of a 2 μm -length suspended CNT. The G^+ mode shows no downshift with applied electric field. Reproduced from Bushmaker et al.⁷² with permission from American Chemical Society. Copyright 2007.

Compared to optical heating, the electrical heating rate can be obtained readily. However, it is nontrivial to extract a thermal property from electrically biased, high-quality CNTs because preferential coupling between the hot electrons with optical phonons can drive the phonon populations out of local thermal equilibrium.^{71,73} For example, Fig. 13 (Ref. 71) shows the Raman shift and the temperature profile for a 5 μm -long suspended CNT [Figs. 13(a) and 13(b)] and another 2 μm -long [Fig. 13(c)] suspended CNT, measured with 0 and 1.2 V bias voltage. The G^+ and G^- phonon peaks were attributed to the transverse optical (TO) and longitudinal optical (LO) phonon modes of metallic nanotubes. For the long nanotube, electrical heated with 1.2 V, both phonon modes are excited to a similar temperature by the energetic electrons. However, for the short nanotube in Fig. 13(c), only one of the peaks downshifts, in this case the G^- peak, with the applied electric bias. The lower temperature profile in Fig. 13(c) is expected to be an upper bound to the lattice temperature, and thus while the G^- mode exists at a high effective temperature, the lattice remains at room temperature. Such local nonequilibrium in the phonon temperature in short CNTs is explained by the slow decay of the hot optical phonons into other phonon modes.

The nonequilibrium issue is less a problem in longer, suspended CNTs. The thermal conductivities of electrically biased, long suspended SWCNTs and MWCNTs have been obtained by Li et al.⁶³ with the use of micro-Raman spectroscopy. The CNTs were grown over 40 μm -deep trenches with two patterned Mo electrodes on either end of the CNT, allowing for electrical heating of the CNT. Based on the Raman G peak position shift, the CNT temperature was probed with the Raman laser at the ends and middle of the suspended sample, and the difference in temperature was used to find the thermal conductivity from the measured electrical heating power and the dimensions of the sample. The effects of contact resistance can be eliminated from the temperature rise measured by the contact. One concern in the measurement of the long suspended nanotube of a small diameter is the radiation loss. Li et al.⁶³ estimated that the radiation loss was < 1% of the heating power. The small radiation loss is due to the small emissivity and large thermal conductivity of the high-quality CNT. Despite these progresses, the limited temperature sensitivity of the Raman techniques requires that the CNT be heated to a rather high temperature during the measurement, and the temperature dependence of the thermal conductivity cannot be resolved with sufficient accuracy, especially at low temperatures.

Further work by Hsu et al.⁷⁴ has investigated the dependence of the gas environment on the heat dissipation

pation from electrically biased suspended SWCNTs. They found a much lower temperature rise in CNTs heated within a gas environment, with 50 - 60% of the Joule heating being conducted away by the surrounding gas. This effect was particularly pronounced for a CO₂ environment and other polyatomic gas molecules with lower thermal conductivity. The results are attributed to the coupling between the hot surface optical phonons of the CNT and the molecular vibration modes of the surrounding polyatomic molecules. Using a two-laser technique, Hsu et al.⁷⁵ further measured the heat transfer coefficient between SWCNT bundles and the surrounding air environment. A suspended CNT bundle with diameters on the order of tens of microns and suspended lengths as long as 89 μm was heated locally with a 750 nm spot size laser. A second laser was incident on the CNT for probing the spatially resolved Raman spectra with resolution up to 1 μm. With the same laser heating power, the maximum temperature increase was 150 K for irradiation in air, compared to 275 K in vacuum. The heat transfer coefficient between the CNT and surroundings was found from the fin heat transfer solution, and ranged from 0.15 to 7.91×10^4 W/m²K. The heat dissipation to the surrounding air is found to be the dominant path of heat transfer for CNT bundles longer than 7 μm. The results suggest the importance of performing thermal conductivity measurements of CNTs, especially defective CNTs of low thermal conductivity, in a vacuum environment.

10 Time Domain Thermoreflectance

Time domain thermoreflectance (TDTR) has been an increasingly popular method for characterization of the thermal property of thin films and interfaces. There have also been reported TDTR measurements on aligned InAs NW-polymer composites,⁷⁶ from which the average thermal conductivity of the individual NWs in the composite can be obtained. InAs NW arrays were grown by chemical beam epitaxy on an InAs substrate, followed by embedding the entire NW array in polymethyl methacrylate (PMMA). To ensure contact with the deposited 90 nm Al film, the PMMA was etched by ozone plasma until the tips of the vertically aligned NWs were just above the PMMA surface. The estimated void fraction in the NW composite was estimated to be < 2%. A laser pulse with duration < 0.3 ps was used to heat the sample, while a probe pulse was used to measure the change in reflectance of the top Al film. The thermal penetration depth of the heating pulse depends on its frequency f as $d = \sqrt{\kappa_C/\pi C_C f}$, where κ_C is the composite thermal conductivity, and C_C is the composite specific heat. It was found that the thermal conductivity of the composite depended on this modulation frequency, which they attribute to a transition between two limits of the NW/PMMA and NW/Al interface conductance: an effective medium limit at low frequency and a two-temperature limit in which the NWs are thermally insulated from the PMMA at high frequencies. The thermal conductivity of the InAs component of the sample can be found from the low-frequency thermal conductivity of the composite from the effective medium theory,

$$\kappa_C = x\kappa_{NW} + (1-x)\kappa_{PMMA} \quad (26)$$

with the thermal conductivity of PMMA (κ_{PMMA}) determined from a separate experiment, and the packing fraction of NWs, x , determined from SEM. This results in a room temperature thermal conductivity for individual InAs NWs of 5.3 Wm⁻¹K⁻¹, which is consistent with another measurements of individual InAs NWs with the use of a suspended resistance thermometer device.⁷⁷

11 Summary and Outlook

A number of experimental methods have been explored in the past decade to address the challenge in thermal and thermoelectric transport measurements of NWs and nanotubes. As discussed above, these methods are based on measurements of either steady state or transient temperature rise and heat flow in NW samples that are heated either externally or internally. For temperature measurements in these experiments, one popular technique is based on microscale resistance thermometers, including suspended Pt serpentines, metal hotwires, or the use of the NW itself as a resistance thermometer. Bimaterial cantilevers have also been employed as temperature sensors in thermal conductivity measurement of NWs. In addition, noncontact optical measurement techniques such as micro-Raman spectroscopy and thermal reflectance measurements have been investigated for determining the temperature drop or temperature distribution in the NW sample. Although thermocouple sensors are commonly used in bulk thermal conductivity measurements and there have been reports of encouraging progress in quantitative nanoscale temperature mapping

with the use of scanning thermal microscopy (SThM) techniques based on microfabricated thermocouple probes,^{78–80} thermocouple sensors have remained to be explored for NW thermal property measurements. Among these temperature measurement techniques, resistance thermometers and bimaterial cantilevers can provide superior temperature sensitivity but limited spatial resolution compared to measurements based on microfabricated thermocouples and optical thermometry techniques. The development of new temperature measurement techniques with enhanced temperature sensitivity and spatial resolution and reduced parasitic heat loss are essential for addressing several challenging problems still present in existing techniques for NW measurements.

One common problem in existing techniques is the error caused by contact thermal resistance. Efforts have been made to overcome this problem by determining the respective temperature drop across the suspended segment of the NW and at the contacts to the NW with the use of the four-probe thermoelectric measurement technique, measuring the length dependence of the NW thermal resistance, or measuring the spatial profile of the temperature distribution along the NW with the use of the micro-Raman spectroscopy technique. Quantitative nanoscale SThM and other novel thermal imaging techniques that provide improved spatial resolution and temperature sensitivity compared to micro-Raman spectroscopy may find use in addressing the contact thermal resistance problem. Furthermore, in transient measurements of thermal diffusivity, the measured thermal time constant of the sample is relatively insensitive to the contact thermal resistance,⁴⁹ providing another powerful set of techniques for thermal characterization.

Another challenging problem in thermal measurement of individual NWs is the determination of the actual heat flow rate in the sample. Thermal measurement techniques based on optical heating of the sample can benefit from new methods for accurate determination of the optical absorption of the sample. In addition, radiation loss from long NWs of small diameter needs to be evaluated adequately.

Besides the challenges in measuring the contact thermal resistance and the actual heat flow rate in the sample, accurate determinations of the cross-sectional area and crystal structure of the NW sample are essential for obtaining high-fidelity thermal conductivity values and for correlating the results with the crystal structure. For a NW sample with an irregular or rough surface, the cross section and thermal conductivity are not well defined. Hence, comparing the thermal conductivity between rough and smooth NWs is nontrivial.

Although progress has been made in obtaining thermal conductivity, Seebeck coefficient, and electrical conductivity of individual NWs, there is still a lack of experimental methods for probing the fundamental transport parameters in individual NWs. There have been some efforts in extracting the electrochemical potential, charge carrier concentration, and mobility from field-effect measurements^{15,81,82} or thermoelectric measurements^{27,83} of individual NWs. However, measurements of phonon dispersion and lifetime in NWs have remained to be explored, and have not been achieved with the use of inelastic neutron scattering and X-ray scattering techniques established for bulk crystals, because the crystal size needs to be sufficiently large for these techniques. Knowledge of these fundamental phonon and electron transport parameters are critically needed to understand the many intriguing experimental results of thermal conductivity, Seebeck coefficient, and electrical conductivity of individual NWs. Hence, the current limited experimental capability calls for innovative approaches for probing thermal and thermoelectric transport in individual NWs.

12 Acknowledgement

The authors thank Profs. Alexis Abramson, Chris Dames, and Deyu Li, and Drs. Michael T. Pettes and Arden L. Moore for helpful discussion. The authors also acknowledge funding support from the National Science Foundation (NSF), Department of Energy, and Office of Naval Research. AW is supported by a NSF Graduate Research Fellowship.

13 References

1. Y. Li, F. Qian, J. Xiang, and C. M. Lieber, Nanowire electronic and optoelectronic devices, *Mater. Today*, **9**:18-27, 2006.
2. R. Agarwal and C. M. Lieber, Semiconductor nanowires: optics and optoelectronics, *Appl. Phys. A*, **85**:209-215, 2006.

3. R. Yan, D. Gargas, and P. Yang, Nanowire photonics, *Nat. Photon.*, **3**:569-576, 2009.
4. R. Martel, T. Schmidt, H. R. Shea, T. Hertel, and P. Avouris, Single- and multi-wall carbon nanotube field-effect transistors, *Appl. Phys. Lett.*, **73**:2447-2449, 1998.
5. S. J. Tans, A. R. M. Verschueren, and C. Dekker, Room-temperature transistor based on a single carbon nanotube, *Nature*, **393**:49-52, 1998.
6. T. Someya, J. Small, P. Kim, C. Nuckolls, and J. T. Yardley, Alcohol vapor sensors based on single-walled carbon nanotube field effect transistors, *Nano Lett.*, **3**:877-881, 2003.
7. Y. Cui, Z. Zhong, D. Wang, W. U. Wang, and C. M. Lieber, High performance silicon nanowire field effect transistors, *Nano Lett.*, **3**:149-152, 2003.
8. D. Hisamoto, W.-C. Lee, J. Kedzierski, H. Takeuchi, K. Asano, C. Kuo, E. Anderson, T.-J. King, J. Bokor, and C. Hu, FinFET-a self-aligned double-gate MOSFET scalable to 20 nm, *IEEE Trans. Electron Devices*, **47**:2320-2325, 2000.
9. X. Huang, W.-C. Lee, C. Kuo, D. Hisamoto, L. Chang, J. Kedzierski, E. Anderson, H. Takeuchi, Y.-K. Choi, K. Asano, V. Subramanian, T.-J. King, J. Bokor, and C. Hu, Sub-50 nm P-channel FinFET, *IEEE Trans. Electron Devices*, **48**:880-886, 2001.
10. E. Pop and K. E. Goodson, Thermal phenomena in nanoscale transistors, *J. Electron. Packag.*, **128**:102-108, 2006.
11. D. G. Cahill, W. K. Ford, K. E. Goodson, G. D. Mahan, A. Majumdar, H. J. Maris, R. Merlin, and S. R. Phillpot, Nanoscale thermal transport, *J. Appl. Phys.*, **93**:793-818, 2003.
12. C. J. Vineis, A. Shakouri, A. Majumdar, and M. G. Kanatzidis, Nanostructured thermoelectrics: Big efficiency gains from small features, *Adv. Mater.*, **22**:3970-3980, 2010.
13. L. D. Hicks and M. S. Dresselhaus, Effect of quantum-well structures on the thermoelectric figure of merit, *Phys. Rev. B*, **47**:12727-12731, 1993.
14. G. D. Mahan and J. O. Sofo, The best thermoelectric, *Proc. Natl. Acad. Sci.*, **93**:7436-7439, 1996.
15. J. Heremans and C. M. Thrush, Thermoelectric power of bismuth nanowires, *Phys. Rev. B*, **59**:12579-12583, 1999.
16. A. Henry, G. Chen, S. J. Plimpton, and A. Thompson, 1D-to-3D transition of phonon heat conduction in polyethylene using molecular dynamics simulations, *Phys. Rev. B*, **82**:144308, 2010.
17. R. P. Tye, *Thermal Conductivity*, Academic Press, New York, 1969.
18. T. S. Tighe, J. M. Worlock, and M. L. Roukes, Direct thermal conductance measurements on suspended monocrystalline nanostructures, *Appl. Phys. Lett.*, **70**:2687-2689, 1997.
19. K. Schwab, E. A. Henriksen, J. M. Worlock, and M. L. Roukes, Measurement of the quantum of thermal conductance, *Nature*, **404**:974-977, 2000.
20. K. Schwab, J. L. Arlett, J. M. Worlock, and M. L. Roukes, Thermal conductance through discrete quantum channels, *Physica E*, **9**:60-68, 2001.
21. L. G. C. Rego and G. Kirczenow, Quantized thermal conductance of dielectric quantum wires, *Phys. Rev. Lett.*, **81**:232-235, 1998.
22. L. Shi, Mesoscopic Thermophysical measurements of microstructures and carbon nanotubes, PhD Thesis, University of California-Berkeley, 2001.
23. P. Kim, L. Shi, A. Majumdar, and P. L. McEuen, Thermal transport measurements of individual multiwalled nanotubes, *Phys. Rev. Lett.*, **87**:215502, 2001.

24. L. Shi, D. Li, C. Yu, W. Jang, D. Kim, Z. Yao, P. Kim, and A. Majumdar, Measuring thermal and thermoelectric properties of one-dimensional nanostructures using a microfabricated device, *J. Heat Transfer*, **125**:881-888, 2003.
25. D. Li, Y. Wu, P. Kim, L. Shi, P. Yang, and A. Majumdar, Thermal conductivity of individual silicon nanowires, *Appl. Phys. Lett.*, **83**:2934-2936, 2003.
26. A. Mavrokefalos, M. T. Pettes, F. Zhou, and L. Shi, Four-probe measurements of the in-plane thermoelectric properties of nanofilms, *Rev. Sci. Instrum.*, **78**:034901, 2007.
27. F. Zhou, J. Szczech, M. T. Pettes, A. L. Moore, S. Jin, and L. Shi, Determination of transport properties in chromium disilicide nanowires via combined thermoelectric and structural characterizations, *Nano Lett.*, **7**:1649-1654, 2007.
28. J. Yang, Y. Yang, S. W. Waltermire, X. Wu, H. Zhang, T. Gutu, Y. Jiang, Y. Chen, A. A. Zinn, R. Prasher, T. T. Xu, and D. Li, Enhanced and switchable nanoscale thermal conduction due to van der Waals interfaces, *Nat. Nano.*, **7**:91-95, 2012.
29. A. Mavrokefalos, A. L. Moore, M. T. Pettes, L. Shi, W. Wang, and X. Li, Thermoelectric and structural characterizations of individual electrodeposited bismuth telluride nanowires, *J. Appl. Phys.*, **105**:104318, 2009.
30. M. T. Pettes and L. Shi, Thermal and structural characterizations of individual single-, double-, and multi-walled carbon nanotubes, *Adv. Funct. Mater.*, **19**:3918-3925, 2009.
31. J. Zhou, C. Jin, J. H. Seol, X. Li, and L. Shi, Thermoelectric properties of individual electrodeposited bismuth telluride nanowires, *Appl. Phys. Lett.*, **87**:133109, 2005.
32. D. Tham, C. Y. Nam, and J. E. Fischer, Microstructure and composition of focused-ion-beam-deposited Pt contacts to GaN nanowires, *Adv. Mater.*, **18**:290-294, 2006.
33. Y. Long, Z. Chen, W. Wang, F. Bai, A. Jin, and C. Gu, Electrical conductivity of single CdS nanowire synthesized by aqueous chemical growth, *Appl. Phys. Lett.*, **86**:153102, 2005.
34. A. Motayed, A. V. Davydov, M. D. Vaudin, I. Levin, J. Melngailis, and S. N. Mohammad, Fabrication of GaN-based nanoscale device structures utilizing focused ion beam induced Pt deposition, *J. Appl. Phys.*, **100**:024306, 2006.
35. V. Gopal, E. A. Stach, V. R. Radmilovic, and I. A. Mowat, Metal delocalization and surface decoration in direct-write nanolithography by electron beam induced deposition, *Appl. Phys. Lett.*, **85**:49-51, 2004.
36. J. Tang, H.-T. Wang, D. H. Lee, M. Fardy, Z. Huo, T. P. Russell, and P. Yang, Holey silicon as an efficient thermoelectric material, *Nano Lett.*, **10**:4279-4283, 2010.
37. A. Weathers, A. L. Moore, M. T. Pettes, D. Salta, J. Kim, K. Dick, L. Samuelson, H. Linke, P. Caroff, and L. Shi, Phonon transport and thermoelectricity in defect-engineered InAs nanowires, *Proc. MRS Spring Meeting*, vol. 1404, MRS Online Library, Cambridge, 2012.
38. C. Yu, S. Saha, J. Zhou, L. Shi, A. M. Cassell, B. A. Cruden, Q. Ngo, and J. Li, Thermal contact resistance and thermal conductivity of a carbon nanofiber, *J. Heat Transfer*, **128**:234- 239, 2006.
39. A. L. Moore and L. Shi, On errors in thermal conductivity measurements of suspended and supported nanowires using micro-thermometer devices from low to high temperatures, *Meas. Sci. Technol.*, **22**:015103, 2011.
40. C. Dames and G. Chen, 1 omega, 2 omega, and 3 omega methods for measurements of thermal properties, *Rev. Sci. Instrum.*, **76**:124902, 2005.
41. M. C. Wingert, Z. C. Y. Chen, E. Dechaumphai, J. Moon, J.-H. Kim, J. Xiang, and R. Chen, Thermal conductivity of Ge and Ge-Si core-shell nanowires in the phonon confinement regime, *Nano Lett.*, **11**:5507-5513, 2011.

42. N. Ashcroft and N. D. Mermin, *Solid State Physics*, Brooks/Cole, Belmont, CA, pp. 523-528, 1976.
43. M. P. Marder, *Condensed Matter Phys.*, Wiley, Hoboken, 2000.
44. K. Hippalgaonkar, B. Huang, R. Chen, K. Sawyer, P. Ercius, and A. Majumdar, Fabrication of microdevices with integrated nanowires for investigating low-dimensional phonon transport, *Nano Lett.*, **10**:4341-4348, 2010.
45. J. Yang, Y. Yang, S. W. Waltermire, T. Gutu, A. A. Zinn, T. T. Xu, Y. Chen, and D. Li, Measurement of the intrinsic thermal conductivity of a multiwalled carbon nanotube and its contact thermal resistance with the substrate, *Small*, **7**:2334-2340, 2011.
46. M. Fujii, X. Zhang, H. Xie, H. Ago, K. Takahashi, T. Ikuta, H. Abe, and T. Shimizu, Measuring the thermal conductivity of a single carbon nanotube, *Phys. Rev. Lett.*, **95**:065502, 2005.
47. C. Dames, S. Chen, C. T. Harris, J. Y. Huang, Z. F. Ren, M. S. Dresselhaus, and G. Chen, A hot-wire probe for thermal measurements of nanowires and nanotubes inside a transmission electron microscope, *Rev. Sci. Instrum.*, **78**:104903, 2007.
48. S. Shen, A. Henry, J. Tong, R. Zheng, and G. Chen, Polyethylene nanofibres with very high thermal conductivities, *Nat. Nanotechnol.*, **5**:251-255, 2010.
49. M. T. Demko, Z. Dai, H. Yan, W. P. King, M. Cakmak, and A. R. Abramson, Application of the thermal flash technique for low thermal diffusivity micro/nanofibers, *Rev. Sci. Instrum.*, **80**:036103, 2009.
50. A. Narayanaswamy, S. Shen, and G. Chen, Near-field radiative heat transfer between a sphere and a substrate, *Phys. Rev. B*, **78**:115303, 2008.
51. H. S. Carslaw and J. C. Jaeger, *Heat Conduction in Solids*, 2nd ed., Oxford University Press, New York, 1959.
52. D. G. Cahill, Thermal conductivity measurement from 30 to 750 K: the 3 omega method, *Rev. Sci. Instrum.*, **61**:802-808, 1990.
53. L. Lu, W. Yi, and D. L. Zhang, 3 omega method for specific heat and thermal conductivity measurements, *Rev. Sci. Instrum.*, **72**:2996-3003, 2001.
54. W. Yi, L. Lu, Z. Dian-lin, Z. W. Pan, and S. S. Xie, Linear specific heat of carbon nanotubes, *Phys. Rev. B*, **59**:R9015-R9018, 1999.
55. M. N. Ou, T. J. Yang, S. R. Harutyunyan, Y. Y. Chen, C. D. Chen, and S. J. Lai, Electrical and thermal transport in single nickel nanowire, *Appl. Phys. Lett.*, **92**:063101, 2008.
56. J. S. Heron, T. Fournier, N. Mingo, and O. Bourgeois, Mesoscopic size effects on the thermal conductance of silicon nanowire, *Nano Lett.*, **9**:1861-1865, 2009.
57. S. Dhara, H. S. Solanki, A. P. R, V. Singh, S. Sengupta, B. A. Chalke, A. Dhar, M. Gokhale, A. Bhattacharya, and M. M. Deshmukh, Tunable thermal conductivity in defect engineered nanowires at low temperatures, *Phys. Rev. B*, **84**:121307, 2011.
58. T.-Y. Choi, D. Poulikakos, J. Tharian, and U. Sennhauser, Measurement of the thermal conductivity of individual carbon nanotubes by the four-point three- ω method, *Nano Lett.*, **6**:1589- 1593, 2006.
59. J. Guo, X. Wang, and T. Wang, Thermal characterization of microscale conductive and non-conductive wires using transient electrothermal technique, *J. Appl. Phys.*, **101**:063537, 2007.
60. B. Feng, W. Ma, Z. Li, and X. Zhang, Simultaneous measurements of the specific heat and thermal conductivity of suspended thin samples by transient electrothermal method, *Rev. Sci. Instrum.*, **80**:064901, 2009.
61. X. Huang, J. Wang, G. Eres, and X. Wang, Thermophysical properties of multi-wall carbon nanotube bundles at elevated temperatures up to 830 K, *Carbon*, **49**:1680-1691, 2011.

62. J. Guo, X. Wang, D. B. Geohegan, G. Eres, and C. Vincent, Development of pulsed laser-assisted thermal relaxation technique for thermal characterization of microscale wires, *J. Appl. Phys.*, **103**:113505, 2008.
63. Q. Li, C. Liu, X. Wang, and S. Fan, Measuring the thermal conductivity of individual carbon nanotubes by the Raman shift method, *Nanotechnology*, **20**:145702, 2009.
64. Y. Yue, G. Eres, X. Wang, and L. Guo, Characterization of thermal transport in micro/nanoscale wires by steady-state electro-Raman-thermal technique, *Appl. Phys. A*, **97**:19-23, 2009.
65. I. K. Hsu, R. Kumar, A. Bushmaker, S. B. Cronin, M. T. Pettes, L. Shi, T. Brintlinger, M. S. Fuhrer, and J. Cumings, Optical measurement of thermal transport in suspended carbon nanotubes, *Appl. Phys. Lett.*, **92**:063119, 2008.
66. A. A. Balandin, S. Ghosh, W. Z. Bao, I. Calizo, D. Teweldebrhan, F. Miao, and C. N. Lau, Superior thermal conductivity of single-layer graphene, *Nano Lett.*, **8**:902-907, 2008.
67. W. W. Cai, A. L. Moore, Y. W. Zhu, X. S. Li, S. S. Chen, L. Shi, and R. S. Ruoff, Thermal transport in suspended and supported monolayer graphene grown by chemical vapor deposition, *Nano Lett.*, **10**:1645-1651, 2010.
68. C. Faugeras, B. Faugeras, M. Orlita, M. Potemski, R. R. Nair, and A. K. Geim, Thermal conductivity of graphene in corbino membrane geometry, *ACS Nano*, **4**:1889-1892, 2010.
69. M. Soini, I. Zardo, E. Uccelli, S. Funk, G. Koblmuller, A. Fontcuberta i Morral, and G. Abstreiter, Thermal conductivity of GaAs nanowires studied by micro-Raman spectroscopy combined with laser heating, *Appl. Phys. Lett.*, **97**:263107, 2010.
70. I. K. Hsu, M. T. Pettes, A. Bushmaker, M. Aykol, L. Shi, and S. B. Cronin, Optical absorption and thermal transport of individual suspended carbon nanotube bundles, *Nano Lett.*, **9**:590-594, 2009.
71. V. V. Deshpande, S. Hsieh, A. W. Bushmaker, M. Bockrath, and S. B. Cronin, Spatially resolved temperature measurements of electrically heated carbon nanotubes, *Phys. Rev. Lett.*, **102**:105501, 2009.
72. A. W. Bushmaker, V. V. Deshpande, M. W. Bockrath, and S. B. Cronin, Direct observation of mode selective electron-phonon coupling in suspended carbon nanotubes, *Nano Lett.*, **7**:3618-3622, 2007.
73. M. Oron-Carl and R. Krupke, Raman spectroscopic evidence for hot-phonon generation in electrically biased carbon nanotubes, *Phys. Rev. Lett.*, **100**:127401, 2008.
74. I. K. Hsu, M. T. Pettes, M. Aykol, L. Shi, and S. B. Cronin, The effect of gas environment on electrical heating in suspended carbon nanotubes, *J. Appl. Phys.*, **108**:084307, 2010.
75. I. K. Hsu, M. T. Pettes, M. Aykol, C.-C. Chang, W.-H. Hung, J. Theiss, L. Shi, and S. B. Cronin, Direct observation of heat dissipation in individual suspended carbon nanotubes using a two-laser technique, *J. Appl. Phys.*, **110**:044328, 2011.
76. A. I. Persson, Y. K. Koh, D. G. Cahill, L. Samuelson, and H. Linke, Thermal conductance of InAs nanowire composites, *Nano Lett.*, **9**:4484-4488, 2009.
77. F. Zhou, A. L. Moore, J. Bolinsson, A. Persson, L. Froberg, M. T. Pettes, H. Kong, L. Rabenberg, P. Caroff, D. A. Stewart, N. Mingo, K. A. Dick, L. Samuelson, H. Linke, and L. Shi, Thermal conductivity of indium arsenide nanowires with wurtzite and zinc blende phases, *Phys. Rev. B*, **83**:205416, 2011.
78. J. Chung, K. Kim, G. Hwang, O. Kwon, S. Jung, J. Lee, J. W. Lee, and G. T. Kim, Quantitative temperature measurement of an electrically heated carbon nanotube using the null-point method, *Rev. Sci. Instru.*, **81**:114901, 2010.
79. K. Kim, J. Chung, J. Won, O. Kwon, J. S. Lee, S. H. Park, and Y. K. Choi, Quantitative scanning thermal microscopy using double scan technique, *Appl. Phys. Lett.*, **93**:3, 2008.

80. I. Jo, I. K. Hsu, Y. J. Lee, M. M. Sadeghi, S. Kim, S. Cronin, E. Tutuc, S. K. Banerjee, Z. Yao, and L. Shi, Low-frequency acoustic phonon temperature distribution in electrically biased graphene, *Nano Lett.*, **11**:85-90, 2011.
81. Y.-M. Lin and M. S. Dresselhaus, Determination of carrier density in Te-doped Bi nanowires, *Appl. Phys. Lett.*, **83**:3567-3569, 2003.
82. J. Small and P. Kim, Thermopower measurement of individual single walled carbon nanotubes, *Micromechanical Thermophys. Eng.*, **8**:1-5, 2004.
83. J. H. Seol, A. L. Moore, S. K. Saha, F. Zhou, L. Shi, Q. L. Ye, R. Scheffler, N. Mingo, and T. Yamada, Measurement and analysis of thermopower and electrical conductivity of an indium antimonide nanowire from a vapor-liquid-solid method, *J. Appl. Phys.*, **101**:023706, 2007.